POLITECNICO DI TORINO

MASTER's Degree in AUTOMOTIVE ENGINEERING



MASTER's Degree Thesis

Simulation-Based Optimisation of Additive Manufacturing Process Parameters for Accurate Polymer Gear Production

Supervisors

Candidate

Prof. Carlo ROSSO

Muhammad Reza OLIAEE

Prof. Cristiana DELPRETE

Ing. Daniele CATELANI

October 2025

Ing. Raffaele RUSSO

Simulation-Based Optimisation of Additive Manufacturing Process Parameters for Accurate Polymer Gear Production

Muhammad Reza Oliaee

Abstract

In collaboration with MSC Software Italia - Hexagon, this thesis aims to leverage finite element simulation to implement a workflow for enhancing the dimensional accuracy of additively manufactured polymer parts. Specifically, the production gears out of polyamide 12 (PA12), using fused filament fabrication (FFF) and selective laser sintering (SLS) technologies, are studied.

The study begins with a comprehensive literature review to identify the process parameters that significantly affect warpage, followed by the establishment of an appropriate testing range for these parameters. To efficiently design the simulation experiments, the Taguchi method is employed for the design of experiments (DOE), enabling a systematic investigation of parameter interactions. A full factorial DOE is also implemented for the application of annealing when needed.

The Digimat AM software is utilised to simulate the manufacturing process, and the resulting shape deviation and residual stresses are evaluated through a thermomechanical study and a viscoelastic material model. This data is collected and fed to a MATLAB script, developed to analyse the results using analysis of variance (ANOVA) techniques, assess the statistical significance of the data, and determine the influence of each parameter along with its optimal level to minimise deformation.

Finally, compensated geometries are generated for samples manufactured with the determined process settings to compensate for the predicted geometrical inaccuracies. After cycles of compensated geometry generation are carried out, a final simulation determines the ultimate obtained shape, which is digitally examined, based on ISO 1328 guidelines, to estimate the tooth flank tolerance class that can be reached.

ACKNOWLEDGMENTS

I would like to thank MSC Software Italia — Hexagon for providing access to the Digimat software and the training on its use, which was essential for carrying out this work.

I am grateful to Ing. Daniele Catelani for his guidance and support throughout the process, and to Ing. Raffaele Russo for his supervision and technical expertise in ensuring the quality of the simulations.

Table of Contents

1	Inti	roduction	1
	1.1	Background and Motivation	1
	1.2	Objectives of the Thesis	2
	1.3	Scope and Limitations	2
	1.4	Structure of the Thesis	3
2	Lite	erature Review	4
	2.1	Overview of Additive Manufacturing	4
		2.1.1 Overview of Polymer AM Technologies	4
	2.2	Warpage in Additive Manufacturing	5
	2.3	Process Parameters Influencing Warpage	6
		2.3.1 Parameters Common to Polymer AM Processes	6
		2.3.2 Process-Specific Parameters in FFF	7
		2.3.3 Process-Specific Parameters in SLS	8
		2.3.4 Interdependence of Parameters:	8
		2.3.5 Link to the present methodology	9
	2.4	Annealing	10
	2.5	Previous Simulation and Optimisation Approaches in AM	10
	2.6	Additive Manufacturing of polymer gears	11
3	Me	thodology	12
	3.1	Software Tools Used	12
		3.1.1 Digimat	12
		3.1.2 MATLAB	14
		3.1.3 Minitab	14
		3.1.4 Autodesk Inventor	15
		3.1.5 UltiMaker Cura	15
	3.2	Description of Gear Models	15
	3.3	Simulation Setup and Assumptions	17
4	Des	ign of Experiments	20
	4.1	Introduction to the Taguchi Method	20
	4.2	Selection of factors and levels	21
	4.3	Orthogonal Array Design	23

$TABLE\ OF\ CONTENTS$

	4.4	Execution of Simulation Runs
5	Ana	alysis of Results
	5.1	Overview of Statistical Tools
	5.2	FFF Simulation Results
		5.2.1 Raw Simulation Results
		5.2.2 Signal-to-Noise Ratio Computation
		5.2.3 Main Effects Plots
		5.2.4 Factor Ranking (Delta Method)
		5.2.5 Analysis of Variance
		5.2.6 Probability Plots
		5.2.7 Optimal Parameter Levels
		5.2.8 Confirmation of the Optimal Settings
	5.3	SLS Simulation Results
		5.3.1 Raw Simulation Results
		5.3.2 Signal-to-Noise Ratio Computation
		5.3.3 Main Effects Plots
		5.3.4 Factor Ranking (Delta Method)
		5.3.5 Analysis of Variance
		5.3.6 Probability Plots
		5.3.7 Optimal Parameter Levels
		5.3.8 Confirmation of the Optimal Settings
6	Res	sidual Stress and Deformation Mitigation
Ū	6.1	Annealing Simulation Results
	6.2	Statistical Analysis of Annealing Parameters
	0.2	6.2.1 Signal-to-Noise Ratio Computation
		6.2.2 Analysis of Variance
	6.3	
	6.4	Overview of Geometry Compensation
	6.5	Implementation of the Geometry Compensation Cycles
	6.6	Evaluation of Compensation Effectiveness
	6.7	Extension to Large Helical Gear
	6.8	Conclusion
7	ISO	Tolerance Evaluation of Manufactured Gears
•	7.1	Introduction
	7.2	Measurement Requirements
	7.3	Class-Based Tolerance Calculation
	7.4	Shape deviation measurements
	1.1	7.4.1 Single and Cumulative Pitch Deviation
		7.4.2 Profile Deviation, Total
		7.4.3 Helix Deviation, Total
		7.4.4 Achieved Tolerance Classes

$TABLE\ OF\ CONTENTS$

	7.5	Extension to the Helical Gears	69
	7.6	Conclusion	69
8	Cor	nclusions and Future Work	71
	8.1	Summary of Findings	71
	8.2	Contributions of the Thesis	72
	8.3	Suggestions for Future Research	73
	8.4	Closing Remarks	74
\mathbf{Bi}	bliog	graphy	7 5
De	edica	ations	80

List of Figures

3.1	Process parameters optimization workflow (adapted from Digimat-AM	
	User Guide [36])	12
3.2	Warpage compensation workflow (adapted from Digimat-AM User	
	Guide [36])	13
3.3	Spur gear model	16
3.4	Helical gear model	16
3.5	Example of Cura-generated toolpath for the spur gear	18
3.6	Example of voxel mesh used for the FFF spur gear simulation	18
3.7	Example of voxel mesh used for the thermal-pass SLS spur gear simulation	19
3.8	Example of voxel mesh used for the SLS simulation with the compen-	
	sated geometry	19
5.1	Main effects plot for warpage S/N ratios in FFF	32
5.2	Main effects plot for total deformation S/N ratios in FFF	33
5.3	Main effects plot for residual stress S/N ratios in FFF	33
5.4	Probability plot for warpage in FFF (pre-annealing)	37
5.5	Probability plot for total deformation in FFF (pre-annealing)	38
5.6	Probability plot for residual stress in FFF (pre-annealing)	38
5.7	Main effects plot for warpage S/N ratios in SLS	42
5.8	Main effects plot for total deformation S/N ratios in SLS	42
5.9	Main effects plot for residual stress S/N ratios in SLS	42
5.10	Probability plot for warpage in SLS	46
5.11	Probability plot for total deformation in SLS	46
5.12	Probability plot for residual stress in SLS	47
6.1	Surface plot showing total deformation of annealed samples	49
6.2	Surface plot showing residual stress in annealed samples	49
6.3	Exaggerated visualisation of deformation of the annealed FFF part $.$	52
6.4	Compensated geometry from FFF simulations	53
6.5	Exaggerated visualisation of deformation in SLS part	53
6.6	Compensated geometry from SLS simulations	54
6.7	Effect of compensated geometries of deformation reduction in FFF	
	snur gear	55

LIST OF FIGURES

6.8	Effect of compensated geometries of deformation reduction in FFF	
	spur gear	55
6.9	Effect of compensated geometries of deformation reduction in SLS	
	spur gear	56
6.10	Comparison of deformed meshes between the base geometry and the	
	compensated geometry for the FFF process	56
6.11	Comparison of deformed meshes between the base geometry and the	
	compensated geometry for the SLS process	57
6.12	Effect of compensated geometries of deformation reduction in FFF	
	helical gear	57
6.13	Effect of compensated geometries of deformation reduction in FFF	
	helical gear	58
6.14	Exaggerated deformation visualisation on the FFF helical gear vox-	
	elized mesh	58
6.15	Visualisation of the voxelized mesh generated for the FFF helical gear.	
	The red surface indicates a need for support structures	59
6.16	Deformation on the bottom face of the helical gear realised by FFF .	60
6.17	The effect of annealing on the residual stress in the helical gear manu-	
	factured by SLS	60
6.18	Exaggerated visualisation of the effect of annealing on the deformation	
	of the helical gear manufactured by SLS	61
6.19	Total deviation from the as-designed geometry in SLS helical gear:	
	before geometry compensation and after four cycles of geometry com-	
	pensation	61
8.1	The effect of the degree of sintering on geometry compensation	74

List of Tables

4.1	Test levels of FFF process parameters	21
4.2	Constant FFF process parameters	21
4.3	Test levels of SLS process parameters	22
4.4	Constant SLS process parameters	22
4.5	Test levels of annealing parameters	23
4.6	DOE based on Taguchi L27 orthogonal array for FFF	23
4.7	Full factorial DOE for SLS	24
4.8	Full factorial DOE for annealing	25
5.1	Simulation results for FFF (pre-annealing)	29
5.2	Signal-to-noise ratios for FFF simulation results	30
5.3	Ranking of FFF process parameters by their influence on warpage	
	S/N ratios	34
5.4	Ranking of FFF process parameters by their influence on total defor-	
	mation S/N ratios	34
5.5	Ranking of FFF process parameters by their influence on residual	
	stress S/N ratios	34
5.6	Analysis of variance for warpage S/N ratios in FFF	35
5.7	Relative contribution of each FFF process parameter to warpage S/N	
	ratios	35
5.8	Analysis of variance for total deformation S/N ratios in FFF	36
5.9	Relative contribution of each FFF process parameter to total defor-	
	mation S/N ratios	36
	Analysis of variance for residual stress S/N ratios in FFF	36
5.11	Relative contribution of each FFF process parameter to residual stress	
	S/N ratios	37
5.12	Most robust parameter levels to minimise warpage and total deforma-	
	tion in FFF	39
	Most robust parameter levels to minimise residual stress in FFF	39
	Confirmation of the optimal process parameters for FFF	39
	Simulation results for SLS (pre-annealing)	40
	Signal-to-noise ratios for SLS simulation results	41
5.17	Ranking of SLS process parameters by their influence on warpage S/N	
	ratios	43

$LIST\ OF\ TABLES$

5.18	Ranking of SLS process parameters by their influence on total defor-	
	mation S/N ratios	43
5.19	Ranking of SLS process parameters by their influence on residual stress S/N ratios	43
5 20	Analysis of variance for warpage S/N ratios in SLS	44
	Relative contribution of each SLS process parameter to warpage S/N	11
0.21	ratios	44
5 22	Analysis of variance for total deformation S/N ratios in SLS	44
	Relative contribution of each SLS process parameter to total deformation S/N ratios	45
F 94	,	
	Analysis of variance for residual stress S/N ratios in SLS	45
5.25	Relative contribution of each SLS process parameter to residual stress	4 -
- 00	S/N ratios	45
	Most robust parameter levels to minimise warpage in SLS	47
	Most robust parameter levels to minimise total deformation in SLS .	47
5.28	Most robust parameter levels to minimise residual stress in SLS	47
6.1	Simulation results for FFF (post-annealing)	48
6.2	Signal-to-noise ratios for annealing simulation results	50
6.3	Analysis of variance for warpage S/N ratios in FFF post-annealing .	51
6.4	Analysis of variance for total deformation S/N ratios in FFF post-	
	annealing	51
6.5		51
6.6	Maximum deviation from the reference geometry in the annealed spur	
	gear after successive compensation cycles in the FFF process	55
6.7	Maximum deviation from the reference geometry in the spur gear after	
	successive compensation cycles in the sls process	56
6.8	Maximum deviation from the reference geometry in the annealed	
	helical gear after successive compensation cycles in the FFF process	58
6.9	Maximum deviation from the reference geometry in the annealed	
	helical gear after successive compensation cycles in the SLS process .	62
7.1	Summary of flank tolerances	64
7.2	Geometrical characteristics of the spur gear	65
7.3	Calculated tolerance values for tooth flank tolerance classes 711	65
7.4	Measured pitch and single pitch deviation (f_{pi}) for each tooth of the	
	spur gear produced by FFF	66
7.5	Measured pitch and single pitch deviation (f_{pi}) for each tooth of the	
	spur gear produced by SLS	66
7.6	Summary of pitch deviations in the spur gear	67
7.7	Measured profile deviation F_{α} for SLS and FFF parts	67
7.8	Summary of profile deviations in the spur gear	67
7.9	Measured profile deviation F_{β} for SLS and FFF parts	68
7.10	Summary of helix deviations in the spur gear	68

$LIST\ OF\ TABLES$

7.11	Tolerance	classes	for	SLS.												69
7.12	Tolerance	classes	for	FFF												69

Acronyms

ABS Acrylonitrile butadiene styrene.

AED Area Energy Density.

AM Additive Manufacturing.

ANOVA Analysis of Variance.

CAD Computer Aided Design.

DOE Design of Experiment.D.F. Degree of Freedom.

FDM Fused Deposition Modelling.FEM Finite Element Method.FFF Fused Filament Fabrication.

mean Sq. Mean Square.

OA Orthogonal Array.

PA12 Polyamide 12.

RVE Representative Volume Element.

SLM Selective Laser Melting.

SLA Stereolithography.

SLS Selective Laser Sintering.

Sum Sq. Sum of Squares.

VED Volumetric Energy Density.

Chapter 1

Introduction

1.1 Background and Motivation

Additive manufacturing (AM) is an innovative fabrication technique that constructs structures and complex geometries by successively layering materials based on three-dimensional model data. This process, first developed by Charles Hull in 1986 through a method called stereolithography (SLA), has since evolved to include various technologies such as powder bed fusion and fused deposition modelling. Initially utilised for prototyping in architecture and design due to its rapid and cost-effective nature, AM later further expanded into diverse industries, including construction and biomedical fields [1].

Additive manufacturing has since advanced to produce both polymer and metal components with high structural integrity, making it suitable for the fabrication of functional products. This leads to the use of AM in the automotive industry, where the sector is being transformed by enabling faster product development, greater design flexibility, and on-demand customisation. Techniques such as fused filament fabrication and selective laser sintering were adopted for prototyping and soft tooling at first. Now, AM plays a critical role across the automotive supply chain. It is used to produce specialised assembly tools, optimised injection moulds through selective laser melting (SLM), and lightweight structural components made possible by generative design and lattice structures. High-performance automotive sectors like Formula 1 and NASCAR were early adopters, benefiting from AM's capacity to produce optimised, performance-driven components. Although the high cost of AM currently limits its widespread use to low-volume or high-end models, the growing demand for mass customisation and lightweight solutions—especially in the context of energy efficiency and alternative propulsion systems—is rapidly expanding its industrial feasibility [2].

Dimensional inaccuracies in additive manufacturing can arise from several key factors. First, the surface quality inherent to the chosen manufacturing technique often leads to deviations from the intended dimensions, as the layer-by-layer process can introduce surface roughness and irregularities that affect overall accuracy. Second, shrinkage due to the cooling of the part is a significant contributor; as materials

solidify and cool, they contract, which can result in parts being smaller than their original design specifications. Third, warpage frequently occurs because of uneven cooling rates and the presence of complex geometries, leading to deformation and further dimensional errors. These effects are well-documented in the literature and represent primary challenges in achieving high precision with AM technologies [3, 4].

Gears are an excellent choice for this thesis because their performance relies heavily on precise geometry, and guidelines for measuring their dimensional accuracy are clearly defined by the ISO standards. The complex tooth profiles and strict tolerances inherent to spur and helical gears make them particularly sensitive to manufacturing defects such as warpage and distortion. By focusing on these components, the study can effectively evaluate how additive manufacturing-induced deformations impact mechanical functionality and assess the potential of simulation-based methods to predict and compensate for such inaccuracies.

1.2 Objectives of the Thesis

The aim of this work is to:

- Identify and evaluate the level of influence of key process parameters on warpage in PA12 parts manufactured by SLS and FFF methods through finite element method (FEM), including the effects of annealing when needed.
- Apply the Taguchi method to optimise those parameters efficiently.
- Develop a MATLAB-based tool to analyse simulation results using statistical methods.
- Generate compensated gear geometries that account for predicted warpage, improving dimensional accuracy.
- Simulate the additive manufacturing of spur and helical gear samples using the optimised parameters and compensated geometry, assessing the final parts' tolerance class according to ISO 1328.

1.3 Scope and Limitations

This thesis focuses on the computational study of dimensional accuracy in gears produced via additive manufacturing. The work investigates two specific technologies, SLS and FFF, applied to Polyamide 12 parts. Using finite element simulations, the study evaluates the influence of process parameters and annealing on warpage, residual stresses, and dimensional accuracy. The scope includes the application of statistical methods for parameter analysis, the generation of compensated geometries, and the verification of gear tolerance class digitally according to ISO 1328 standards.

This thesis investigates the application of FEM simulations to analyse gears produced via Additive Manufacturing, with emphasis on SLS and FFF. The work is

purely computational, without physical manufacturing or experimental validation. The build chamber dimensions do not correspond to a specific printer, and a uniform chamber temperature is assumed, omitting real, machine-specific thermal gradients and process qualification. In practice, a variable chamber temperature field must be defined based on the specific machine that will be used. The heat radiation from the deposition head is also neglected in the study of the FFF process.

The material properties provided by the DIGIMAT library for PA12 are used, incorporating relaxation effects and viscoelastic behaviour, but assuming isotropic and homogeneous properties.

In FFF, the material deposition is modelled layer-by-layer rather than using the filament deposition approach. Fine mesh size is used whenever possible, but a medium mesh is employed for the larger gear, as the size increases the computational power required. In any case, mesh sensitivity analysis is carried out, ensuring good simulation quality.

In SLS, the full powder bed is simulated, but a coarse mesh is used for the thermal pass to limit the required computational resources. ISO gear tolerance standards are applied digitally by measuring deformed STL geometries in Autodesk Inventor Professional rather than physically. Surface roughness, porosity, process-induced defects, and other secondary effects evaluated by Digimat-AM are not considered.

1.4 Structure of the Thesis

This thesis is organised as follows:

- Chapter 2 presents a literature review on warpage in additive manufacturing, process parameters and the optimisation of them, and the use of simulation techniques relevant to polymer AM.
- Chapter 3 describes the methodology, including the simulation setup, gear geometries, and the software tools employed.
- Chapter 4 details the Design of Experiments using the Taguchi method, including the selection of factors and levels and the resulting parameter combinations.
- Chapter 5 provides an in-depth analysis of the simulation results, examining statistical significance, factor effects, and warpage modelling.
- Chapter 6 focuses on optimisation strategies, annealing trials, and the design of compensated geometries for warpage mitigation.
- Chapter 7 presents the final simulations and validation of the optimised parameters and compensated designs.
- Chapter 8 concludes the thesis with a summary of findings, contributions, and suggestions for future research directions.

Chapter 2

Literature Review

2.1 Overview of Additive Manufacturing

The ISO/ASTM 52900 terminology standard defines additive manufacturing, commonly known as 3D printing, as the process of making parts directly from 3D model data by joining materials. Parts are usually formed in a layer-by-layer sequence that, in comparison to traditional subtractive manufacturing, realises the part by adding material where it is needed instead of removing material to obtain the desired shape.

The origins of AM trace back to the 1980s, starting with stereolithography, and since then, the technology has evolved significantly, expanding into various techniques and material domains [1]. The key principle underlying AM is the sequential addition of material in layers, based on a computer model of the object, allowing for the realisation of complex shapes, higher efficiency in material usage, and faster production in the absence of tooling. Hence, additive manufacturing initially gained popularity as rapid prototyping, enabling the easy production of visual prototypes. Since then, advancements in AM materials have allowed their application not only to produce functional prototypes but also end-user products.

2.1.1 Overview of Polymer AM Technologies

Different AM processes for polymer parts can be summarised as:

- Photopolymerization: This group of processes uses lasers, lamps, or UV light projectors to cure and solidify liquid photopolymer resins layer by layer. Key techniques include Stereolithography, which relies on a laser, and Digital Light Processing, which utilises light projection. Parts obtained by these processes offer high surface and aesthetic quality, making them ideal for visual prototypes [5, 6].
- Material Jetting: Droplets of photopolymer material are jetted and cured by UV light. This process, similar to inkjet printing, enables high-precision, multi-material printing with good surface finish [7].
- Binder Jetting: This technique uses a bed of polymer or ceramic powder, onto which droplets of binder are selectively jetted, forming what is known as a

green part. This part is then post-processed to increase mechanical properties by improving coalescence and material density. This technique allows for high build speed without the need for high production temperatures [8].

- Selective Laser Sintering: Also known as powder bed fusion, this process uses a laser beam to selectively melt layers of pre-heated powder to realise the shape of each layer. A complex interplay between process parameters determines the degree of coalescence within and between each layer, ultimately affecting the geometric quality and mechanical properties of the part. SLS is one of the methods studied in this work, as it is capable of printing functional parts [9].
- Material Extrusion: Probably the most well-known additive manufacturing technique, it involves melting a thermoplastic filament that is deposited by an extruder to form each layer. This technique can be cost-effective and versatile, supporting a wide material range and used by both hobbyists and professionals. Machines are available with a broad range of prices, controls, and resulting print quality, as well as compatibility with a wide range of materials. This technique will also be included in this work [10].

2.2 Warpage in Additive Manufacturing

Warpage refers to the geometric distortion of a manufactured part from the intended as-designed form. It is primarily caused by non-uniform shrinkage during cooling, and it is a major issue in AM processes such as FFF and SLS, in which thermoplastic polymers experience high temperatures and melting. Warpage is an important consideration for functional components since it undermines dimensional accuracy, mechanical performance, and assembly tolerance [11, 12].

Thermal gradients during the repeated heating-cooling cycles inherent to these processes are the main cause of the phenomenon. As deposited material cools from the melt state, it contracts; in semi-crystalline polymers, such as polypropylene and polyamide 6, crystallisation intensifies this volumetric change. Amorphous polymers, such as acrylonitrile butadiene styrene and polycarbonate, generally shrink less due to their gradual glass transition. Shrinkage is anisotropic in layered parts, driven by polymer chain orientation and non-uniform temperature fields, leading to residual stresses that manifest as bending or twisting [12, 13, 14].

Warpage is influenced by process-specific parameters. In FFF, poor adhesion of the first layer, differences in the cooling rate of different layers, and the build orientation affect the distribution of residual stresses. In SLS, uneven energy input or non-uniform powder bed temperature can cause local contractions. Geometry also plays a role: thin walls, overhangs, and asymmetric shapes are more susceptible to distortion than dense, compact forms. Environmental stability, particularly chamber temperature control, is equally important in reducing thermal gradients and associated stresses [11, 12].

In order for the parts to fit and function properly, warpage must be controlled to ensure dimensional tolerances are respected. Surface quality is also affected, and distortions can often cause visible defects, harming the part's appearance. In addition, the presence of residual stress can reduce mechanical performance [12].

Accurate prediction of warpage allows for effective process optimisation in AM. Numerical simulation enables assessment of residual stresses, temperature distribution, and deformations before fabrication. This helps reduce costs as process parameters such as chamber and bed temperatures, energy input, and build orientation can be tuned without costly trial-and-error experimentation [11, 12].

2.3 Process Parameters Influencing Warpage

In fused filament fabrication and selective laser sintering techniques, warpage is a common issue that stems from the residual stress build-up caused by the repeated heating and cooling of successive layers. As new material is deposited and cools down, differential shrinkage and non-uniform temperature fields develop, making it impossible to obtain parts free of internal stresses. Therefore, it is necessary to optimise the process parameters to minimise warpage. In the following paragraphs, the key process parameters governing SLS and FFF processes are identified through a review of the scientific literature. In FFF, typical parameters included extrusion temperature, layer thickness, deposition speed, infill density, and bed temperature. Meanwhile, in the SLS process, chamber temperature, laser power and scanning speed, plus the scanning pattern and hatch spacing, play the most prominent roles [14, 13, 15, 16, 17].

2.3.1 Parameters Common to Polymer AM Processes

- Build orientation and placement: Positioning of the part inside the build chamber changes the thermal history and spatial variability of the material properties. Regarding the warpage, corners and edges often suffer from greater distortion. This problem can be counteracted by processing sequences that delay the sintering of corners. *Printing height*, also determined by the orientation, is reported to have a significant effect on shape deviations [16].
- Layer thickness: In fused filament fabrication, a higher layer thickness extends cooling times, which can increase thermal gradients and shrinkage non-uniformity. Several studies on PA12 material report a positive correlation between layer thickness and warpage. A typical layer thickness for FFF of PA12 is approximately 0.1 mm to 0.3 mm [16, 17, 18].

In selective laser sintering, the effect of layer thickness can be dependent on the material and scanning pattern. When using PA12, one study reports opposite trends when different scanning patterns are used. Meanwhile, for PA12/High-Density Polyethylene (HDPE) blends, a higher layer thickness lowers energy absorption and reduces warping height. A trade-off is often needed, however, to

ensure good interlayer bonding. A typical layer thickness for SLS using PA12 is $0.1 \,\mathrm{mm}$ [11, 15].

- Bed and chamber temperature: First-layer adhesion and thermal gradients are strongly influenced by bed temperature in FFF. It is reported to be the top contributing factor for PA12 (contributing $\sim 81\%$ of total effect), with an optimum near 100 °C (slightly above $T_g \approx 97$ °C), beyond which warpage rose again. In SLS, suitable chamber preheating reduces residual stress, shrinkage, and warping height, but excessive surrounding temperature can increase warpage due to additional energy absorption by the powder [13, 17, 16].
- Cooling rate and deposition history: Residual stresses arise from repeated thermal cycling. Faster depositing speeds in FFF can reduce warpage by shortening the time between passes, enabling annealing from subsequent beads and reducing reheating of prior filaments; inadequate cooling control, however, risks sagging or print failure. Heat transfer involves convection/radiation from exposed surfaces and conduction at bead-bead/bed contacts; viscoelastic relaxation during cooling also contributes to the final stress state [11, 15, 14].
- Geometry and scanning strategy: Thin walls, overhangs, and asymmetric shapes are more susceptible to distortion. In SLS, scan patterns that sinter corners later yield lower residual stresses and warpage than patterns that sinter corners first [16].

2.3.2 Process-Specific Parameters in FFF

- Extrusion temperature: Its relation to warpage is non-linear. For PA12, increasing extrusion temperature from 240 °C to 260 °C reduced warpage, but warpage increased again at 280 °C. Higher temperatures increase inter-bead energy and reheating, steepening thermal gradients and potentially raising residual stresses if outside an optimal window [11].
- **Deposition speed:** Higher deposition speed significantly reduced warpage in PA12 (optimal ~ 100 mm/s). While in CFR—PA12, it also reduced simulated and measured residual stresses. The reason is that by increasing the deposition speed, each layer has less time to cool down before the successive layer is added on top, reducing the reheating of the previous layers, and the temperature gradients between different layers [11, 15].
- Infill density and pattern. For PA12, warpage increased with infill density; a low infill (20%) minimised deformation. Toolpath pattern also governs internal stress distribution, though detailed trends depend on the chosen pattern [11].
- Material: Semi-crystalline polymers exhibit crystallisation—induced volume change and viscosity rise at T_c , affecting interlayer bonding and driving additional strains; additives and reinforcement modify these behaviours [15].

2.3.3 Process-Specific Parameters in SLS

• Energy Density as a Combined Parameter: Area energy density (AED) and volumetric energy density (VED) are common parameters that quantify the energy input in the SLS process.

$$AED = \frac{P}{v \cdot h} \tag{2.1}$$

$$VED = \frac{P}{v \cdot h \cdot t} \tag{2.2}$$

where P is the laser power, v is the scanning speed, h is the hatch spacing, and t is the layer thickness. Appropriate AED values help avoid under- or over-sintering and mitigate distortion. Reported ranges for AED are typically $0.2 \,\mathrm{J\,mm^{-2}}$ to $0.7 \,\mathrm{J\,mm^{-2}}$ [16, 18, 19].

- Laser power and scan speed: For PA12, higher scan speeds generally increased warpage due to reduced sintering width and depth, which enlarged the heat exchange area and raised thermal gradients. The effect of laser power varied, but moderate values often minimised distortion, while excessive power could lead to greater shrinkage. For PA12/HDPE blends, warpage was lowest around 21 W, increasing gradually with higher power. Scan speed also slightly increased warpage in these blends, though the effect was modest [16, 17].
- **Hatch spacing:** Together with power and speed, hatch spacing sets AED; adjustments to maintain constant AED alter heat distribution and thereby warpage [16].
- Powder characteristics: The thermal and morphological properties of the powder determine the layer spread quality and the spreading behaviour, affecting the warpage. PA12 powders used in experiments typically have near spherical shapes, with a narrow size distribution (mean diameter 56–59 µm, range 39–72 µm) and often coated with silica nanoparticles to improve flowability. As a semi-crystalline polymer, PA12 exhibits a glass transition temperature near 50 °C and a melting range of 172–180 °C, with flow properties strongly dependent on processing temperature. Optimal spreading is achieved around 100 °C, while approaching the melting point increases particle cohesion and reduces flow, leading to uneven layers. Poor flow or irregular powder beds can cause local variations in energy absorption during sintering, resulting in non-uniform shrinkage and elevated residual stresses, which ultimately exacerbate warpage [20, 18, 17].

2.3.4 Interdependence of Parameters:

In Fused filament fabrication, the thermal history, material flow, and solidification behaviour are influenced by the joint effect of the discussed parameters. Rather than

acting in isolation, the parameters are interdependent, meaning changes in one might amplify or downplay the effect of another. In the literature, the Taguchi method is commonly used to tune the process parameters for the FFF process, and this thesis also makes use of this methodology.

In Selective laser sintering, the interplay between process parameters is so strong that their individual contributions to part distortion cannot be reliably isolated using simple statistical approaches. Initial attempts using the Taguchi method revealed no clear relation between certain parameters and warpage, largely because designing the experiments using the Taguchi method, while varying all process parameters, leads to some experiments with unrealistically high or low energy densities. Such extremes lead to simulated temperature histories far from actual processing conditions, obscuring true process—property relationships. By instead fixing secondary parameters, constraining the process to realistic conditions, and controlling energy density via laser power, it was possible to reach good print quality.

2.3.5 Link to the present methodology

In this thesis, the selection of process parameters for simulation-based optimisation is guided by the literature reviewed above, ensuring that tested ranges are both practically achievable and relevant to reported material behaviour.

For **FFF**, five factors are varied in the design of experiments:

- Infill density: 20%, 50%, and 90% to capture low, medium, and high structural fill conditions.
- **Deposition speed**: 20, 60, and 100 mm/s, spanning low to high build rates.
- Extrusion temperature: 240 °C, 260 °C, and 280 °C, chosen around typical PA12 melt-processing temperatures.
- Layer thickness: 0.2, 0.3, and 0.4 mm to examine effects on part consolidation and surface finish.
- Bed temperature: 90 °C, 100 °C, and 110 °C, based on maintaining adequate layer adhesion while avoiding overheating.

For **SLS**, two primary factors are varied:

- Chamber temperature: 150 °C, 157.5 °C, 165 °C, 172.5 °C, and 180 °C, covering a range from well below to just under the PA12 melting temperature to assess its effect on residual stresses and powder flow.
- Volumetric energy density: 0.16–0.40 J/mm³, a range chosen to avoid under- to over-sintering conditions.

These defined ranges and step values are implemented in the Taguchi L27 (FFF) and a full factorial L25 (SLS) design to systematically explore parameter effects on output metrics.

2.4 Annealing

Several studies have investigated the effect of annealing on Polyamide 12 (PA12) across different additive manufacturing technologies. Zhao et al. [21] examined SLS-printed PA12 and reported that annealing between 190–230 °C with holding times of 15–30 minutes improved mechanical performance, with an optimum at 210 °C for 15 minutes, where tensile strength reached 57.3 MPa and microstructural defects were reduced. Ferreira et al. [22] studied FFF-printed PA12, annealed at 135–165 °C for 3–18 hours, and found that crystallinity and flexural properties increased significantly, particularly at 135 °C for 3 hours, while higher temperatures (165 °C) led to property degradation.

Liu et al. [23] focused on MJF-printed PA12 and GF/PA12, primarily annealed at 173 °C for 5 hours, and observed tensile strength gains of around 20–23% and modulus increases up to 49%, although elongation at break sharply decreased. Zhang et al. [24] reviewed various studies and concluded that annealing around 150 °C for 3 hours is widely considered effective for PA12, while higher temperatures such as 173 °C can further improve strength at the expense of ductility. Alternative approaches, such as microwave or induction annealing, were also reported to enhance composite PA12 properties.

Since this work aims to study the production of functional parts, when mandated by high values of residual stress, annealing is used to release the internal stresses. A full factorial DOE is used to set annealing time and temperature.

2.5 Previous Simulation and Optimisation Approaches in AM

Finite element modelling has been widely adopted to simulate additive manufacturing processes, particularly for Fused Filament Fabrication and Selective Laser Sintering [25, 26]. However, among the research focusing on warpage, the majority use an experimental approach over the simulation approach. Among the available tools, the Digimat-AM platform is frequently used due to its capability to couple process simulation with multiscale material modelling. This enables the prediction of residual stresses, warpage, and secondary effects by linking microstructural characteristics to macro-scale behaviour.

Several studies have utilised Digimat-AM or other Digimat modules to examine the effect of process parameters on deformation. Sharafi et al. [27] developed a dual-scale modelling approach for FFF, linking representative volume element (RVE) homogenisation to part-scale FEM to predict deflection and strength under varying raster angles and build directions. Alzyod and Ficzere [13, 28] applied Digimat-AM to optimise printing parameters for ABS and PA12, using Taguchi designs to quantify parameter influence on warpage and residual stresses, identifying bed temperature and infill density as dominant factors. Khanjar [29] integrated simulation with design-of-experiments to evaluate warpage reduction strategies in ABS and reinforced

composites, while Al Rashid and Koç [30] focused on the influence of infill patterns and densities, achieving good agreement between simulated and experimental results.

For larger-scale applications, Castelló-Pedrero et al. [31] demonstrated the use of Digimat-AM for large-format additive manufacturing of carbon fibre reinforced polymers, employing digital twins to optimise process settings and minimise distortion. Other works have targeted composite systems, showing that modelling can capture the effect of inclusion geometry, reinforcement type, and fibre orientation on part deformation.

Overall, these studies highlight the capability of FEM-based AM simulation to predict process-induced deformation and optimise process parameters. In the presented study, Digimat-AM was used to simulate both SLS and FFF, enabling a direct comparison between the two processes. The analysis incorporated the annealing process and geometry compensation, which are essential for producing functional parts. Gears with both simple and more complex geometries were considered, allowing the study to focus on practically relevant components and to use ISO standards as guidelines for evaluating acceptable and unacceptable deformations.

2.6 Additive Manufacturing of polymer gears

Past research on polymer gears produced by additive manufacturing techniques primarily focuses on the influence of process parameters, material selection, and post-processing on the mechanical performance and dimensional accuracy. Calignano et al. [32] examined recycled powder use in SLS for the production of PA12 gears and reported that the build orientation and powder reuse significantly affect dimensional accuracy with vertical builds and a high ratio of reused powder leading to potential interference in gear meshing. Zhang et al. [33] applied artificial neural networks coupled with a genetic algorithm to predict and optimise the fatigue life of nylon gears fabricated via FDM, achieving high prediction accuracy and performance gains through parameter tuning. Hriberšek et al. [34] demonstrated that optimising flow rate in FFF carbon-reinforced polyamide gears improved tooth filling, reduced meshing temperatures, and increased fatigue life. Gupta [35] emphasised the advantages of AM for complex gear geometries, while also noting persistent challenges in control-ling deformation, ensuring consistent material properties, and meeting dimensional tolerances.

Chapter 3

Methodology

3.1 Software Tools Used

3.1.1 Digimat

The presented work utilises the Digimat-AM software, version 2024.2, to perform simulations. Digimat-AM is specifically designed for studying additive manufacturing processes using polymers and composite materials [36]. It can simulate selective laser sintering, fused filament fabrication, and fused deposition modelling processes. This software enables the evaluation of temperature history, deformation, residual stresses, and changes in microstructure based on the used material, process parameters, and printing strategies. Its predictive capabilities can help reduce development time and costs by minimising the need for trial-and-error. Figure 3.1 shows the workflow that was used to find the preferred process settings. The simulation type, process type, and the printer dimensions are determined during the *Printing Project* step. In the following Component step, users import the part geometry and the material specifications. The *Manufacturing* step involves setting process parameters, boundary conditions such as temperatures, and tool paths for FFF or FDM processes. In the Solver section, users configure mesh settings and generation parameters, and solver options, including type and time-stepping strategy. The Job Submission tab allows for the selection of the number of processor cores and output file types. Finally, results are generated, visualised, and exported during the *Post-processing* step.

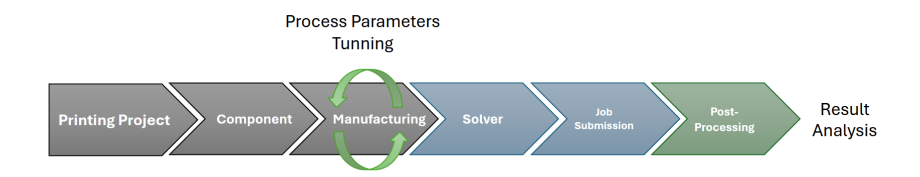


Figure 3.1: Process parameters optimization workflow (adapted from Digimat-AM User Guide [36]).

Additionally, compensated geometries can be generated, based on the obtained deformation simulation results, to minimise the deviation from the intended design.

In this work, the best process settings are obtained first, and then this feature is used to compensate for the residual warpage. Figure 3.2 shows the warpage compensation workflow. The compensated geometry can be generated in the post-processing and must be uploaded in the Manufacturing step of the subsequent simulation.



Figure 3.2: Warpage compensation workflow (adapted from Digimat-AM User Guide [36]).

Digimat-AM provides different levels of simulation fidelity. Available simulation types are thermal, low-fidelity, and high-fidelity analyses to balance computational cost against the needed output and accuracy level. Each of these approaches applies to FFF/FDM and SLS processes, with specific adaptations depending on the technology.

Thermal analysis focuses exclusively on the prediction of the temperature history within the part (and, in the case of SLS, within the surrounding powder bed). It uses a transient solver. Since no mechanical effects are included, it is computationally efficient and primarily suited to studying thermal phenomena such as crystallinity evolution or cooling rate effects.

Low-fidelity analysis introduces mechanical prediction but relies on simplifications to reduce complexity. For FFF/FDM, this is achieved through the inherent strain approach, where precomputed strain fields, either derived from RVEs or calibrated experimentally, are applied during a structural simulation. For SLS, the low-fidelity approach skips explicit powder modelling and assumes full sintering, significantly lowering the computational burden. While faster, these methods are best suited for initial warpage estimation rather than detailed local effects.

High-fidelity analysis, by contrast, performs a full thermomechanical transient simulation of the printing process, incrementally activating elements as the part is deposited or sintered. In FFF/FDM, this may be carried out in filament or layer-by-layer modes, providing highly resolved temperature fields and mechanical responses. The layer-by-layer approach adds entire layers as the simulation proceeds forward, while the filament approach utilises a mesh with a voxel size equal to the layer thickness and adds a portion of a layer, determined by the tool path and deposition speed, when advancing to the next time increment. For SLS, the most rigorous implementation is the full build approach, which explicitly models both the parts and the surrounding powder bed.

The high-fidelity full build simulation in SLS has a two-pass workflow. Firstly, a thermal pass computes the complete temperature history of the powder bed and the parts within it, accurately capturing the thermal interactions between parts and the effect of the surrounding powder. Secondly, a thermomechanical pass maps the previously obtained thermal history onto parts to calculate residual stresses and

warpage.

Pre-defined material properties are chosen from the software's library, where PA12 is available with a thermo-viscoelastic material model including the relaxation effect, taking into account the Prony series of the shear and bulk moduli, thermal expansion, density, conductivity, specific heat capacity, and crystallisation parameters. FFF simulations accounted for key parameters such as extrusion temperature, build plate temperature, bead width, deposition speed, convection coefficient, and annealing temperature and time.

Overall, Digimat-AM provided a robust framework to link process parameters, material behaviour, and resulting part quality, offering valuable insights into additive manufacturing optimisation and reducing the need for extensive experimental testing.

3.1.2 MATLAB

In this work, MATLAB 2025a, together with the Statistics and Machine Learning Toolbox, was employed as the primary computational environment for the design of experiments and result analysis. The toolbox was first used to generate the Taguchi orthogonal arrays corresponding to the selected design of experiments, which provided the systematic and reduced set of parameter combinations that needed to be tested experimentally. MATLAB was then used to organise the collected data into structured tables and to compute signal-to-noise (S/N) ratios according to the smaller-the-better criterion for each quality characteristic under investigation. To evaluate the statistical significance of the observed variations, one-way and multifactor analysis of variance were performed within MATLAB, allowing the identification of the contribution and relative influence of each process parameter on the measured responses. In addition, regression models were built using MATLAB's linear modelling functions, which enabled the establishment of quantitative relationships between the process parameters and the responses. Main effects plots, delta ranking tables, and optimum level identification were also generated directly in MATLAB, providing both numerical and visual insights into sensitivity to parameter and process setting robustness. Overall, MATLAB served as an integrated platform for experimental planning, statistical analysis, and visualisation, ensuring a rigorous, reproducible, and statistically grounded evaluation of the process behaviour.

3.1.3 Minitab

Minitab Statistical Software 22 is a data analysis tool widely used in engineering and research. In this work, it was employed to generate probability plots for assessing the normality of experimental data. The software provides both graphical alignment with a fitted distribution line and associated p-values, which were used to evaluate conformity to statistical assumptions [37].

3.1.4 Autodesk Inventor

Autodesk Inventor Professional 2026 is a computer-aided design (CAD) software widely used in mechanical engineering for creating, simulating, and analysing 3D digital prototypes of mechanical components. It provides advanced modelling tools, assembly simulations, and integrated design validation features, making it a standard platform for both product development and engineering analysis.

In this study, Autodesk Inventor was employed to perform the measurement and evaluation of gear tooth flank deviations, with the aim of checking compliance against ISO standards for gear quality assessment. The ISO standards prescribe specific geometric measurements that must be carried out on manufactured gears in order to determine the flank tolerance class. Since physical manufacturing and direct measurement of printed samples were outside the scope of this thesis, the workflow was adapted by leveraging simulation outputs. Specifically, Digimat was used to export the deformed geometry of the printed gear as an STL file, which was then imported into Autodesk Inventor. Within Inventor, the surface mesh corresponding to the gear tooth flank was selected, and a continuous surface was generated from the mesh data. This process was repeated for both the as-designed and the as-manufactured models. By comparing these reconstructed flank surfaces, it became possible to replicate the ISO-prescribed measurements virtually and assess the deviations between the nominal and deformed geometries. In this way, Autodesk Inventor served as the primary tool for the metrological evaluation of gear flank deviations, enabling a standards-based tolerance analysis without the need for a physically manufactured specimen.

3.1.5 UltiMaker Cura

UltiMaker Cura (version 5.10.0) was used as the slicing software to prepare the toolpaths for the FFF simulations. Cura converts 3D models (in STL format) into printer-readable G-code, which defines the deposition path, speed, and layer thickness. This software was selected because it is free, open-source, and widely adopted in polymer additive manufacturing research. For this work, Cura was employed to generate reproducible toolpaths, ensuring that the simulation setup reflected realistic printing conditions.

3.2 Description of Gear Models

Two gear geometries were designed and used as case studies in this work: a spur gear with profile shift and a helical gear. Both models were provided as STL files and subsequently imported into Autodesk Inventor for inspection and preparation before being used in Digimat-AM simulations.

Spur Gear

The spur gear corresponds to a small gear with a module of $m=3\,\mathrm{mm}$, number of teeth z=11, and a positive profile shift of x=0.3. The face width is $b=10\,\mathrm{mm}$.

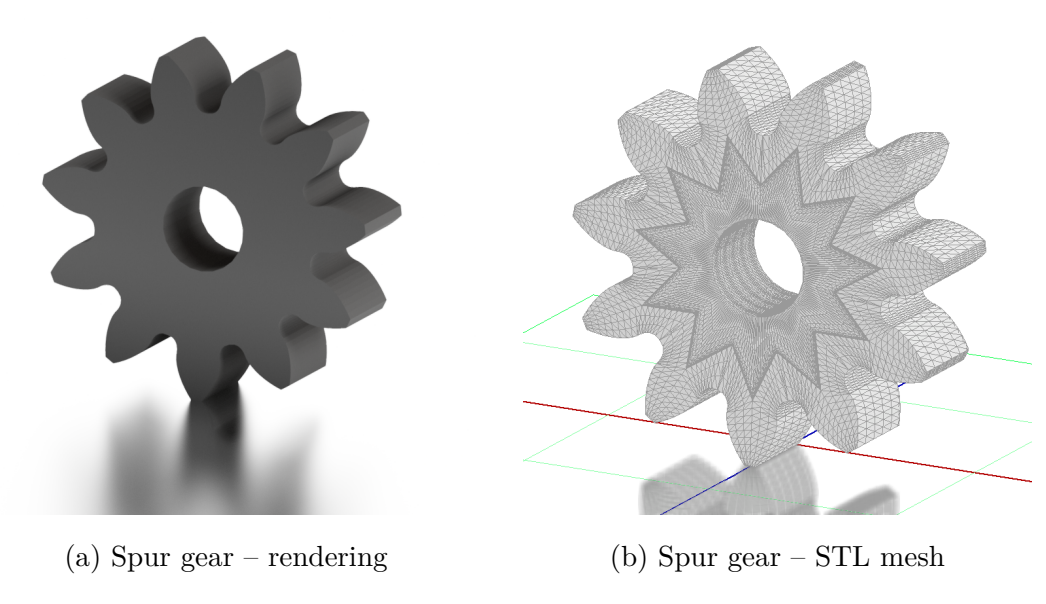


Figure 3.3: Spur gear model

Helical Gear

The second model is a medium-sized helical gear with a module of $m=6\,\mathrm{mm}$, number of teeth z=21, and no profile shift (x=0). The face width is $b=100\,\mathrm{mm}$. And a helical angle of $\beta=28.40^\circ$.

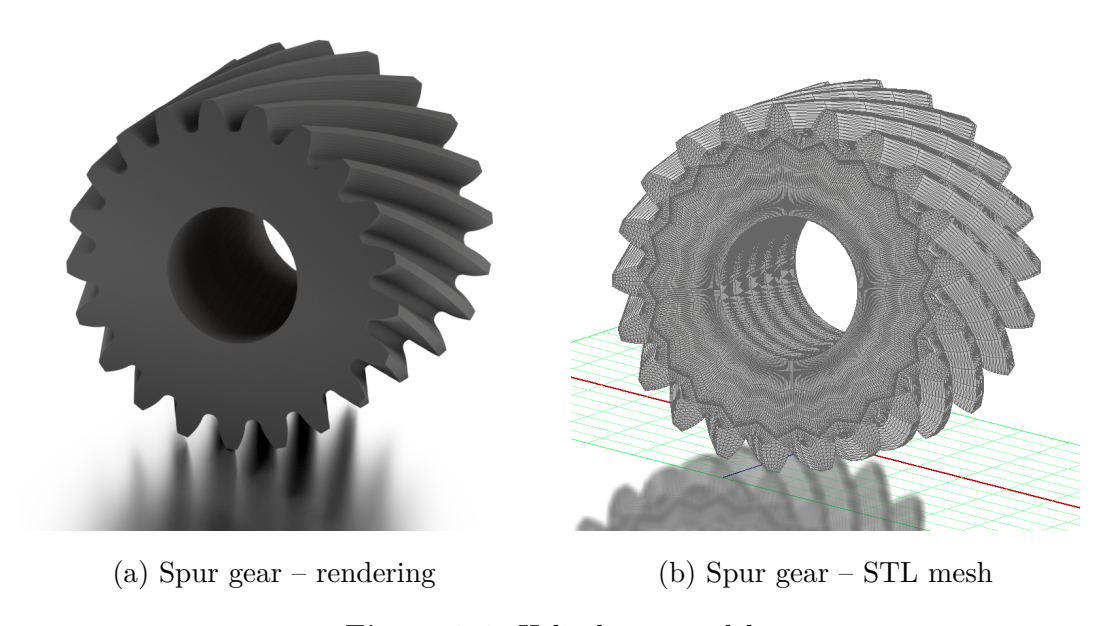


Figure 3.4: Helical gear model

For both gears, non-essential features such as shaft holes, fillets, or chamfers were omitted to reduce computational cost. This ensures that the models capture the

essential geometry relevant for warpage prediction without unnecessary simulation complexity.

3.3 Simulation Setup and Assumptions

As no physical printer was used in this work, a virtual build chamber of $200 \times 200 \times 200 \,\mathrm{mm}^3$ was defined. This is smaller than the default size of $400 \times 400 \times 400 \,\mathrm{mm}^3$, reducing computational cost in full-build simulations while remaining sufficiently large for the chosen gear geometries. All simulations were carried out in high-fidelity mode, with default Digimat-AM settings unless otherwise specified.

For the FFF simulations, the moving-platform configuration was selected. Process parameters were assigned according to the DOE tables and matched to their corresponding toolpaths. The G-code was generated in UltiMaker Cura and imported into the simulation environment.

Key assumptions included a convection coefficient of $15\,\mathrm{W/m^2}\cdot{}^\circ\mathrm{C}$, a bead width of $0.4\,\mathrm{mm}$, and ambient and final temperature of $23\,{}^\circ\mathrm{C}$. The manufacturing sequence consisted of three stages: printing, cooling, and, where applicable, support removal and post-process annealing. No support structures, brims, or skirts were included in the toolpath. Figure 3.5 shows an example of the Cura-generated toolpath for the spur gear at mid-print and after completion.

Discretisation in Digimat-AM is controlled by the voxel size, which is defined relative to the deposited layer thickness. Three refinement levels are typically available: in a coarse mesh, the voxel size is about ten times the layer thickness; in a medium mesh, it is around five times the thickness; and in a fine mesh, the voxel size is reduced to approximately twice the layer thickness.

In this study, the spur gear was meshed with the fine option, while a medium mesh was used for the helical gear to limit computational demand. The default solver was adopted, as no significant variation was observed when comparing to alternative solvers. Mesh convergence was checked by refinement, and only negligible changes were found, justifying the use of coarser meshes when necessary. Figure 3.6 illustrates an example of the FFF mesh for the spur gear. With a layer thickness of 0.2 mm, the voxel size was set to 0.4 mm, resulting in around 116000 voxels.

For the SLS simulations, full-build mode was employed. Default parameters were used for the laser beam diameter (0.5 mm) and number of lasers (1). A convection coefficient of $15\,\mathrm{W/m^2}\cdot$ °C and a constant chamber temperature were assumed, consistent with the FFF setup.

According to the Digimat manual, high-fidelity SLS simulations require two passes: a thermal pass, generally performed with a coarser mesh, followed by a mechanical pass for warpage prediction using a finer mesh. For the spur gear, coarse and medium meshes were applied. For the helical gear, custom voxel sizes of 2.0 and 1.6 mm were defined. These settings produced close to one million voxels, which approached the memory limits of the system; finer meshes could not be attempted.

Mesh sensitivity checks confirmed that further refinement would not significantly

improve accuracy. Figure 3.7 shows a typical SLS thermal-pass mesh for the spur gear. Compared with the FFF mesh in figure 3.6, this mesh uses a medium voxel size, with edges refined by one level of sub-voxelization to better capture geometry. Around 22000 voxels were used to mesh the part itself, while the inclusion of the entire powder bed increased the total voxel count to more than 800000. This explains the higher computational cost and the need for medium voxel sizes. For the second high-fidelity warpage pass, meshes similar to those used in the FFF simulations were applied.

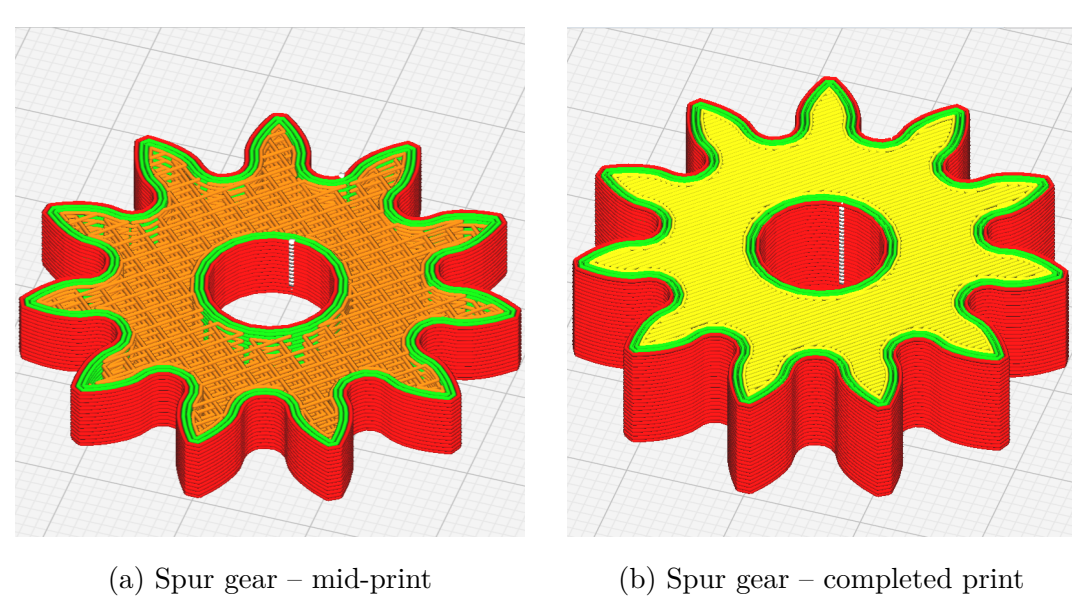


Figure 3.5: Example of Cura-generated toolpath for the spur gear

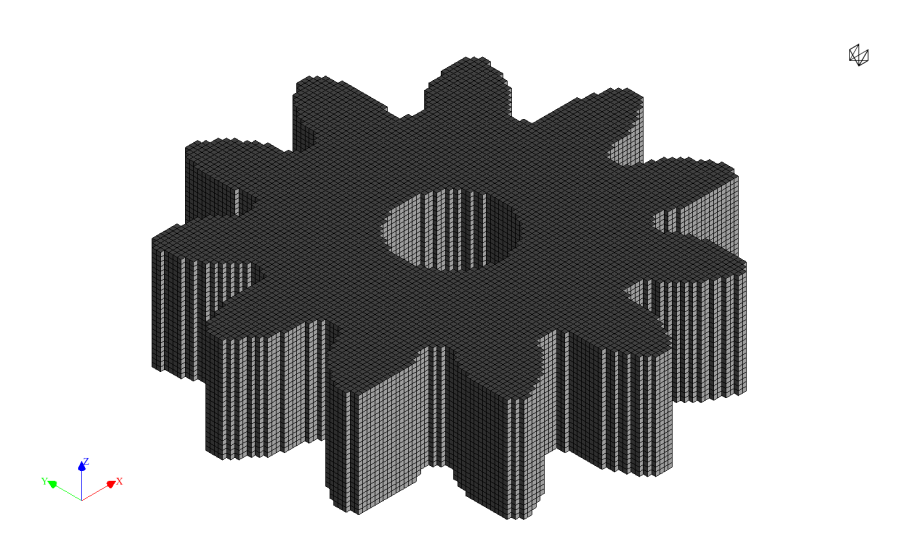


Figure 3.6: Example of voxel mesh used for the FFF spur gear simulation

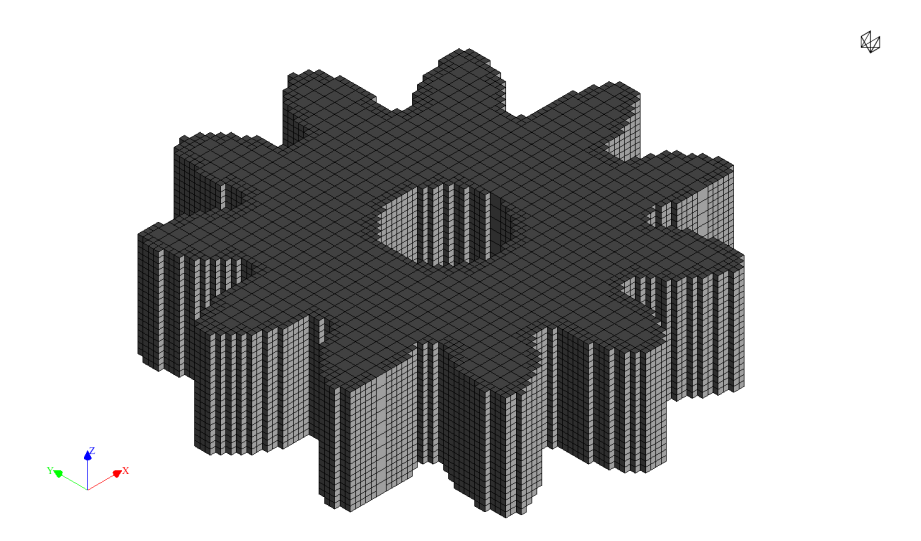


Figure 3.7: Example of voxel mesh used for the thermal-pass SLS spur gear simulation

Figure 3.8 shows the mesh quality used for both thermal and warpage passes of the final SLS simulations with the compensated geometries. It can be seen how the use of sub-voxelization leads to a layer of fine mesh on the surface of the part. This is critical, since the compensated geometry consists of curved surfaces and faces, as opposed to the simpler *as-designed* geometry.

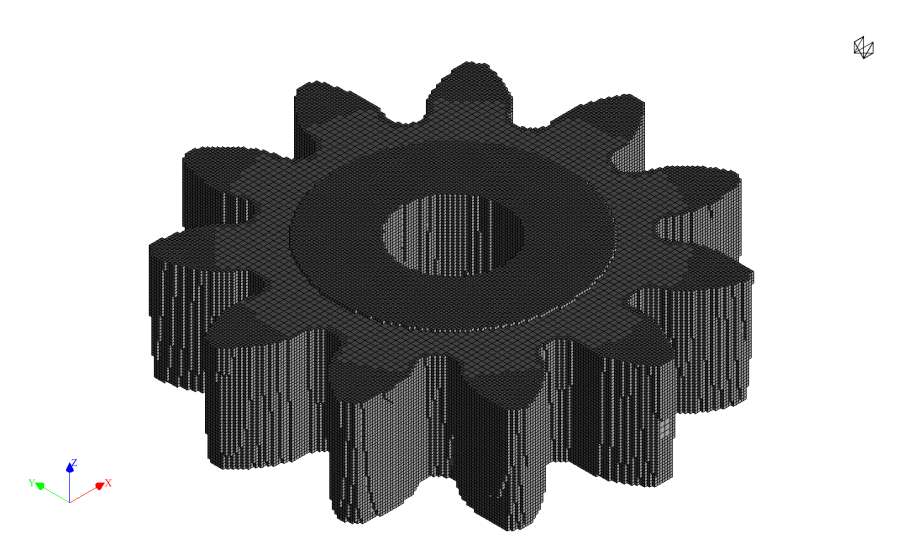


Figure 3.8: Example of voxel mesh used for the SLS simulation with the compensated geometry

Chapter 4

Design of Experiments

4.1 Introduction to the Taguchi Method

Systematic experimentation, rather than ad hoc trial—and—error, is essential in engineering and manufacturing to improve quality and reliability. The framework of *Design of Experiment* provides a structured way to investigate the effects of multiple factors simultaneously. Classical factorial experimentation, inspired by early statistical work in the 1920s, becomes impractical as the number of factors grows: investigating 15 two-level factors would require 2^{15} (32,768) experimental runs, which is prohibitively expensive in both time and resources [38].

In response to these limitations, Dr. Genichi Taguchi developed a statistical methodology that emphasises robust design by building quality into the product or process during its design stage. Rather than attempting to eliminate uncontrollable noise factors, the Taguchi method identifies optimal levels of controllable factors that make the system less sensitive to variation. This robustness is achieved through the use of an outer array design that systematically incorporates noise factors into the experiment [38].

To further simplify experimentation, Taguchi introduced the use of *orthogonal* arrays (OAs), which provide a standardised and efficient means of studying factor effects with a greatly reduced number of runs. For example, instead of the 2¹⁵ trials required for a full factorial design with 15 two-level factors, an appropriately chosen Taguchi OA can reduce the experiment to as few as 16 runs. This not only improves efficiency but also ensures consistency of design across different experimenters [38].

Previous studies have demonstrated the effectiveness of the Taguchi method in additive manufacturing research. For example, Alzyod and Ficzere [11, 13, 28] applied various Taguchi orthogonal arrays (L9 and L27) to optimise printing parameters and minimise warpage deformation in ABS and PA12 parts, as well as to study residual stress and warpage across different materials. Similarly, Ferreira et al. [22] employed a full factorial DOE to investigate the influence of annealing conditions on the mechanical performance of PA12-based specimens. Espino et al.[39] highlighted the Taguchi method as a robust statistical tool for optimising multiple 3D printing parameters and reported its use in studies by Shakeri et al. and Arifin et al. for

improving dimensional accuracy, mechanical behaviour, and hardness. Verim et al.[40] also employed the Taguchi L16 orthogonal array to optimise PLA printing parameters and improve a wide range of mechanical properties. Given this broad evidence of the Taguchi method's applicability and efficiency in handling multiple process variables in fused filament fabrication, and considering the high number of parameters involved in our study, the Taguchi approach was selected to systematically design experiments and identify optimal process conditions. Full factorial DOE is used to study SLS and annealing parameters.

4.2 Selection of factors and levels

Fused Filament Fabrication

Based on the literature review, the five process parameters most frequently reported to influence part quality and dimensional accuracy in FFF were selected for investigation: infill density, deposition speed, layer thickness, extrusion temperature, and bed temperature. These factors have been shown in prior studies to significantly affect mechanical properties, surface finish, and warpage deformation [13, 40, 39].

The selected levels for each parameter, reported in table 4.1, are commonly used in research and include the optimal settings reported by different researchers.

Parameter	Unit	Factor Levels
Infill Density	%	20, 50, 90
Deposition Speed	${ m mms^{-1}}$	20, 60, 100
Layer Thickness	mm	0.20, 0.30, 0.40
Extrusion Tmperature	$^{\circ}\mathrm{C}$	240, 260, 280
Bed Temperature	$^{\circ}\mathrm{C}$	90, 100, 110

Table 4.1: Test levels of FFF process parameters

Other parameters, such as build orientation, chamber temperature, geometry, infill pattern, chamber size, and material, were kept constant throughout the experiments to isolate the effects of the selected variables.

Table 4.2: Constant FFF process parameters

Parameter	Value
Chamber Size	$200 \times 200 \times 200 \text{ mm}^3$
Chamber Temperature	30 °C
Bead Size	$0.4 \mathrm{\ mm}$
Material	PA12
Infill Pattern	Grid
Build Orientation	Horizontal

Selective Laser Sintering

As discussed in Section 2.2, the strong interdependence between SLS process parameters can lead to unrealistic energy inputs when all factors are varied simultaneously. To avoid this issue, chamber temperature and volumetric energy density were selected as the primary variables in this study. Chamber temperature directly influences powder bed preheating and part shrinkage, while VED provides a combined measure of laser power, scan speed, hatch spacing, and layer thickness, and is therefore widely used as a robust indicator of the effective energy input. In this work, VED was controlled through adjustments in laser power. The selected ranges, summarised in table 4.3, were chosen to cover realistic operating windows for PA12 reported in the literature.

Other process parameters, such as scan speed, hatch space, and layer thickness, were kept constant to constrain the process within practical conditions and to isolate the effects of chamber temperature and VED. These fixed parameters, along with machine specifications and part orientation, are listed in table 4.4.

Table 4.3: Test levels of SLS process parameters

Parameter	Unit	Test Levels
Chamber Temperature	$^{\circ}\mathrm{C}$	150, 157.5, 165, 172.5, 180
Volumetric Energy Density	$ m Jmm^{-3}$	0.16,0.22,0.28,0.34,0.40

Table 4.4: Constant SLS process parameters

Parameter	Value
Scan Speed	2000 mm/s
Hatch Spacing	$0.2 \mathrm{\ mm}$
Layer Thickness	0.1 mm
Chamber Size	$200 \times 200 \times 200 \text{ mm}^3$
Part Orientation	Horizontal
Material	PA12
Number of Lasers	One

Annealing

The levels and ranges of annealing parameters were adapted from Ferreira et al. [22], who investigated their influence on the mechanical performance of PA12 and PA12 fibre-reinforced specimens fabricated by fused filament fabrication. In the present work, these parameters were applied to both SLS and FFF parts to identify a trade-off between deformation and residual stress.

Table 4.5: Test levels of annealing parameters

Parameter	Unit	Test Levels
Temperature	$^{\circ}\mathrm{C}$	135, 150, 165
Duration	hours	3, 6, 12, 18

4.3 Orthogonal Array Design

The selection of the parameters, their range, and levels were discussed previously. This section presents the DOE used for each process.

Fused Filament Fabrication

Table 4.6 presents the Taguchi orthogonal array for the FFF process. The selected L27 design systematically varies infill density, deposition speed, extrusion temperature, layer thickness, and bed temperature. This design enables the analysis of both main effects and interactions among these parameters.

Table 4.6: DOE based on Taguchi L27 orthogonal array for FFF

Run	Infill Density (%)	$\begin{array}{c} {\rm Deposition} \\ {\rm Speed} \\ {\rm (mm/s)} \end{array}$	Extrusion Temp. (°C)	Layer thickness (mm)	Bed Temp. (°C)
1	20	20	240	0.2	90
2	20	20	260	0.3	100
3	20	20	280	0.4	110
4	20	60	240	0.3	110
5	20	60	260	0.4	90
6	20	60	280	0.2	100
7	20	100	240	0.4	100
8	20	100	260	0.2	110
9	20	100	280	0.3	90
10	50	20	240	0.2	90
11	50	20	260	0.3	100
12	50	20	280	0.4	110
13	50	60	240	0.3	110
14	50	60	260	0.4	90
15	50	60	280	0.2	100
16	50	100	240	0.4	100
17	50	100	260	0.2	110
18	50	100	280	0.3	90
19	90	20	240	0.2	90
20	90	20	260	0.3	100
21	90	20	280	0.4	110

... continued from previous page

\mathbf{Run}	Infill	Deposition	Extrusion	Layer	\mathbf{Bed}
	$\begin{array}{c} \textbf{Density} \\ (\%) \end{array}$	$egin{array}{c} \mathbf{Speed} \ \mathbf{(mm/s)} \end{array}$	Temp. $(^{\circ}C)$	$rac{ ext{thickness}}{ ext{(mm)}}$	Temp. $(^{\circ}C)$
	(70)	(111111/5)	(C)	(111111)	(0)
22	90	60	240	0.3	110
23	90	60	260	0.4	90
24	90	60	280	0.2	100
25	90	100	240	0.4	100
26	90	100	260	0.2	110
27	90	100	280	0.3	90

Selective Laser Sintering

To investigate the effect of processing conditions in selective laser sintering, a full factorial DOE was employed. As discussed in Section 4.2, chamber temperature and volumetric energy density were chosen as the primary factors, since they capture the main thermal and energy input characteristics of the process while keeping other parameters constant. Five levels were selected for each factor, covering a realistic operating range for PA12.

The DOE thus consisted of 25 experimental runs, enabling the combined influence of chamber temperature and VED on part quality and residual stress to be systematically studied. In addition, the corresponding laser power values were calculated to realise the targeted VED values while holding scan speed, hatch spacing, and layer thickness constant. The complete DOE matrix for the SLS process is presented in table 4.7.

Table 4.7: Full factorial DOE for SLS

Run	Volumetric Energy Density $(J \text{ mm}^{-3})$	Chamber Temp. (°C)	Laser Power (W)
1	0.16	150.0	6.4
2	0.22	150.0	8.8
3	0.28	150.0	11.2
4	0.34	150.0	13.6
5	0.40	150.0	16.0
6	0.16	157.5	6.4
7	0.22	157.5	8.8
8	0.28	157.5	11.2
9	0.34	157.5	13.6
10	0.40	157.5	16.0
11	0.16	165.0	6.4

... continued from previous page

Run	Volumetric	Chamber	Laser
	Energy Density	Temp. ($^{\circ}$ C)	Power
	$(\mathrm{J}\mathrm{mm}^{-3})$		(\mathbf{W})
12	0.22	165.0	8.8
13	0.28	165.0	11.2
14	0.34	165.0	13.6
15	0.40	165.0	16.0
16	0.16	172.5	6.4
17	0.22	172.5	8.8
18	0.28	172.5	11.2
19	0.34	172.5	13.6
20	0.40	172.5	16.0
21	0.16	180.0	6.4
22	0.22	180.0	8.8
23	0.28	180.0	11.2
24	0.34	180.0	13.6
25	0.40	180.0	16.0

Annealing

Table 4.8 summarises the full factorial design for the annealing process. The experiments vary the annealing temperature and duration in a systematic manner, allowing the influence of thermal treatment on part performance to be assessed.

Table 4.8: Full factorial DOE for annealing

Run	$egin{array}{c} ext{Temperature} \ (^{\circ} ext{C}) \end{array}$	Duration (h)
	(0)	(11)
1	135	3
2	135	6
3	135	12
4	135	18
5	150	3
6	150	6
7	150	12
8	150	18
9	165	3
10	165	6
11	165	12
12	165	18

4.4 Execution of Simulation Runs

Each row of the orthogonal arrays (tables 4.6, 4.7, and 4.8) corresponds to a single simulation case. The workflow of the simulation campaign was structured as follows. First, the simulations for the FFF technology were carried out on the spur gear geometry. From these runs, the most robust process settings were identified in order to minimise deformation. Second, with these preferred FFF parameters fixed, the annealing DOE was performed, where annealing time and temperature were varied while keeping the manufacturing settings unchanged. In this way, the most effective annealing conditions were determined. Finally, geometry compensation cycles were executed with the preferred manufacturing and annealing parameters, repeating the procedure until no significant improvement in dimensional accuracy was observed. The resulting deformed geometries were then exported and evaluated to determine the achieved flank tolerance class.

For the SLS process, the same approach was adopted. However, for the spur gear, no annealing was performed since the residual internal stresses were acceptable. Once the preferred settings were identified, the larger helical gear was simulated for both FFF and SLS. For the larger gear in SLS, however, an additional annealing step was required to reduce residual stresses. Compensation cycles were repeated, and the dimensional tolerances of the final geometries were assessed.

In total, 27 runs were conducted for the FFF process, 12 runs for annealing, and 16 runs for SLS. Tool-paths for FFF were generated using Ultimaker Cura according to the parameter settings defined in the DOE. No additional preprocessing was required in *Digimat-AM*, and the same mesh was reused across all runs to ensure consistency, except in cases where the layer thickness was modified, which required re-meshing.

All simulations were executed on a computer equipped with a $13^{\rm th}$ Gen Intel[®] CoreTM i9-13900F CPU (2.00 GHz), 64 GB RAM, and SSD storage.

For each run, *Digimat-AM* provided warpage, total deformation, and the residual von Mises stress distribution. Maximum values of these quantities were recorded and stored in Excel spreadsheets for subsequent processing in MATLAB. For the SLS process, the maximum chamber temperature during each build was also monitored and recorded from the simulation temperature history.

The dataset obtained from these simulation runs forms the input for the analysis and interpretation presented in the next chapter.

Chapter 5

Analysis of Results

5.1 Overview of Statistical Tools

To evaluate the influence of process parameters on the simulation outcomes and to identify suitable settings, several statistical techniques were employed.

As discussed in Chapter 4.1, the Taguchi method was adopted because it provides a systematic and efficient approach to studying multiple parameters simultaneously. By using orthogonal arrays, the method enables robust design: that is, the selection of parameter levels that minimise the influence of uncontrollable factors, often referred to as noise. In this context, robustness means reducing the sensitivity of the results to random variations or unexplained effects, thereby ensuring consistent performance. In the literature, the term optimisation is often used in connection with Taguchi analysis. In this thesis, the term will sometimes be used in the same way, but it should not be confused with mathematical optimisation, which seeks an exact minimum or maximum (e.g., of residual stress). Rather, Taguchi's approach identifies parameter combinations that achieve the most stable and reliable outcome under varying conditions.

For each simulation run, two measures of dimensional deviation were extracted from Digimat-AM:

- **Total deformation**: the overall deflection of the part, including both uniform shrinkage and non-uniform distortions.
- Warpage: computed with respect to the downscaled geometry, isolating the non-uniform distortions by excluding volumetric shrinkage.

In addition, the residual von Mises stress distribution was obtained. For all runs, the *maximum* values of total deformation, warpage, and residual von Mises stress were recorded and tabulated for subsequent analysis.

Signal-to-Noise (S/N) Ratio

The Taguchi method evaluates performance using the signal-to-noise ratio, which expresses the robustness of a response to variation. Depending on the objective,

different formulations exist: larger-the-better, smaller-the-better, and nominal-the-best. In this study, the smaller-the-better criterion was applied for warpage, total deformation, and residual stress. A higher S/N ratio indicates a more favourable and consistent performance of the corresponding factor combination. For a response where smaller values are desirable, the S/N ratio is calculated as:

$$S/N = -10 \cdot \log_{10} \left(\frac{1}{n} \sum_{i=1}^{n} y_i^2 \right)$$
 (5.1)

where n is the number of repetitions and y_i are the observed response values.

Main Effects Plot

Main effects plots are used to visualise how the mean response changes across the levels of each factor. A steeper slope in these plots indicates that the factor has a stronger influence on the outcome. This tool provides a straightforward way to identify which process parameters dominate the response behaviour.

Analysis of Variance

Analysis of Variance was employed to quantify the relative contribution of each process parameter to the variation observed in the responses, namely warpage, total deformation, and residual stress. By decomposing the total variation into components associated with each factor and the residual error, ANOVA identifies which parameters have statistically significant effects. The F-statistic and corresponding p-value are used to determine significance, while the percentage contribution indicates the relative influence of each factor. This analysis, applied to the signal-to-noise (S/N) ratios obtained from the Taguchi design, enables the identification of the most influential parameters and supports the selection of robust settings that minimise variability in the manufacturing process.

In the ANOVA table, the $Sum\ Sq.$ (sum of squares) quantifies the total variation attributed to each factor, while the d.f. (degrees of freedom) corresponds to the number of independent comparisons available for that factor. The $Mean\ Sq.$ (mean square) is obtained by dividing the sum of squares by the corresponding degrees of freedom, and represents the average variation explained by the factor. The F value is the ratio of the factor mean square to the error mean square, providing a statistical measure of the factor's significance. Finally, the Prob>F column reports the p-value, indicating the probability that the observed factor effect could have occurred by chance. Lower p-values therefore denote greater statistical significance.

Probability Plots

Probability plots were used to assess whether the responses (warpage, total deformation, and residual stress) follow a normal distribution. This step is important because many of the statistical tools employed, such as ANOVA, rely on the assumption of normally distributed residuals. In these plots, data points that align closely with

the reference line indicate approximate normality, while larger deviations suggest otherwise.

Two numerical indicators are reported alongside the plots. The Anderson–Darling statistic measures how strongly the data deviate from a normal distribution, with higher values corresponding to poorer fit. The p-value provides a statistical basis for this decision: if the p-value is greater than 0.05, the null hypothesis of normality cannot be rejected, and the data may be treated as normally distributed. When the p-value falls below this threshold, significant deviation from normality is implied.

5.2 FFF Simulation Results

5.2.1 Raw Simulation Results

Table 5.1 presents the maximum values for warpage, total deformation, and stress. These values were obtained from the 27 simulation runs conducted as part of the fused filament fabrication study, which followed the DOE outlined in table 4.6. This data serves as the foundation for the statistical analysis of the process parameters' impact on part performance, which will be discussed in the subsequent section. High levels of residual stress, inherent to the FFF process, are seen. Hence, annealing will also be needed for the production of functional parts.

Table 5.1: Simulation results for FFF (pre-annealing)

Run	Warpage	Total	Stress
	(mm)	deformation	(MPa)
		(mm)	
1	0.4492	0.4365	26.84
2	0.5245	0.4954	16.90
3	0.6018	0.5132	23.37
4	0.4479	0.4817	13.73
5	0.5246	0.4842	19.64
6	0.5837	0.4850	26.92
7	0.4517	0.4646	16.39
8	0.5091	0.4724	23.11
9	0.5810	0.4297	22.48
10	0.4470	0.4661	26.25
11	0.5816	0.5526	30.65
12	0.5976	0.5976	21.89
13	0.5044	0.5299	26.77
14	0.5201	0.5488	18.77
15	0.5798	0.5298	26.51
16	0.4459	0.5320	15.65
17	0.5050	0.5193	22.55

	c		
 . continued	from	previous	page

Run	Warpage (mm)	$egin{array}{c} ext{Total} \ ext{deformation} \ ext{(mm)} \end{array}$	Stress (MPa)
18	0.5915	0.5804	27.90
19	0.4458	0.4779	26.36
20	0.5777	0.5338	27.85
21	0.5915	0.5929	22.25
22	0.4979	0.5224	23.23
23	0.5153	0.5624	19.63
24	0.5786	0.5400	26.87
25	0.4423	0.5473	16.38
26	0.5039	0.5301	23.31
27	0.5799	0.5842	25.60

5.2.2 Signal-to-Noise Ratio Computation

The signal-to-noise (S/N) ratio was used to assess the robustness of the process responses. Since warpage, total deformation, and residual stress follow a *smaller-the-better* criterion, higher ratios indicate more favourable performance.

Table 5.2 lists the computed values based on the raw data in table 5.1. Warpage and total deformation show generally consistent results, with most ratios around 6–7. Runs 12, 15, and 21 stand out as less favourable due to higher deformation and warpage. Residual stress exhibits a wider spread, with negative ratios reflecting deviation from the ideal zero-stress state; here, less negative values correspond to better outcomes. This larger variation suggests residual stress is more sensitive to changes in process parameters compared with deformation..

Table 5.2: Signal-to-noise ratios for FFF simulation results

Run	Warpage S/N (dB)	$\begin{array}{c} {\rm Total} \\ {\rm Deformation} \\ {\rm S/N} \ ({\rm dB}) \end{array}$	Residual Stress S/N (dB)
1	6.9512	7.2003	-28.5757
2	5.6051	6.1009	-24.5577
3	4.4110	5.7943	-27.3732
4	6.9764	6.3445	-22.7534
5	5.6034	6.2995	-25.8628
6	4.6762	6.2852	-28.6015
7	6.9030	6.6584	-24.2916
8	5.8639	6.5138	-27.2760
9	4.7165	7.3367	-27.0359

... continued from previous page

Run	Warpage S/N (dB)	Total Deformation	Residual Stress
	5/N (db)	S/N (dB)	S/N (dB)
10	6.9938	6.6304	-28.3826
11	4.7075	5.1518	-29.7286
12	4.4718	4.4718	-26.8049
13	5.9445	5.5161	-28.5530
14	5.6783	5.2117	-25.4693
15	4.7344	5.5178	-28.4682
16	7.0153	5.4818	-23.8903
17	5.9342	5.6916	-27.0629
18	4.5609	4.7255	-28.9121
19	7.0172	6.4133	-28.4189
20	4.7660	5.4524	-28.8965
21	4.5609	4.5404	-26.9466
22	6.0572	5.6399	-27.3210
23	5.7588	4.9991	-25.8584
24	4.7524	5.3521	-28.5854
25	7.0857	5.2355	-24.2863
26	5.9531	5.5128	-27.3508
27	4.7329	4.6688	-28.1648

5.2.3 Main Effects Plots

The main effects plots were generated to visualise the influence of individual process parameters on warpage, total deformation, and residual stress. These plots illustrate how the average S/N ratio changes with different levels of each factor, allowing the identification of the parameters that most strongly affect part performance. Steeper slopes in the plots indicate greater sensitivity, while flatter lines suggest minimal impact.

Figure 5.1 shows the mean S/N ratio for each of the three levels of the five selected process parameters. Based on these plots, extrusion temperature and layer thickness have the highest effect on warpage, as the largest swings in S/N ratio are observed for these two parameters. This can be explained by the fact that these factors most strongly influence the cooling rate of a newly deposited layer, creating thermal gradients that lead to uneven contraction and warpage. Conversely, infill density appears to be the least sensitive parameter.

It can also be seen that, likely due to the reduction of thermal gradients, higher deposition speeds, lower extrusion temperatures, and lower bed temperatures help reduce the warpage. Figure 5.2, instead, reflects the sensitivity of total deformation to the process parameters. Lower bed temperature, extrusion temperature, layer

thickness, and infill density all have favourable effects. Interestingly, while infill density has the lowest effect on warpage, it shows the highest effect on total deformation when the influence of uniform shrinkage is also considered. Deposition speed, which affects the cooling rate and has a moderate effect on warpage, exhibits the lowest impact on total deformation. In this case, lower layer thickness, bed temperature, and extrusion temperature contribute to reducing total deformation.

The three main contributors to warpage are also the primary contributors to residual stress, which is consistent since both phenomena arise from uneven cooling. Lower infill densities and extrusion temperatures help reduce both warpage and residual stress, while a higher deposition speed is generally preferable. However, although a lower layer thickness is beneficial for minimising warpage and total deformation, it can have a detrimental effect by increasing residual stresses. This occurs because thinner layers cool and solidify more quickly, which traps internal strains before they can relax, leading to higher residual stresses. Figure 5.3 illustrates these trends in the main effects plots, highlighting how each parameter influences residual stress.

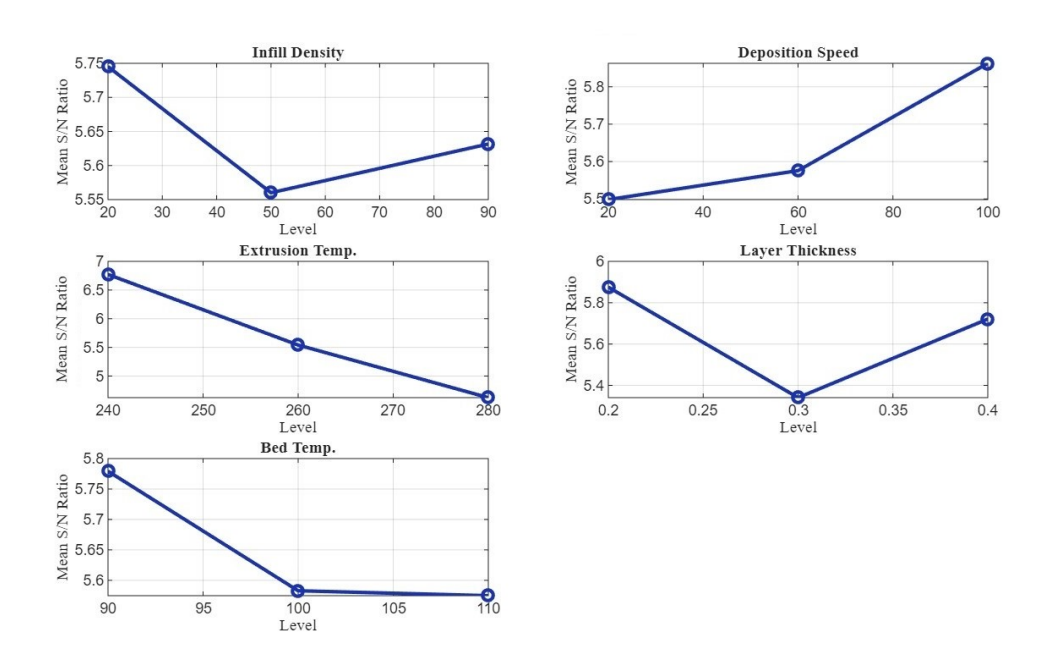


Figure 5.1: Main effects plot for warpage S/N ratios in FFF.

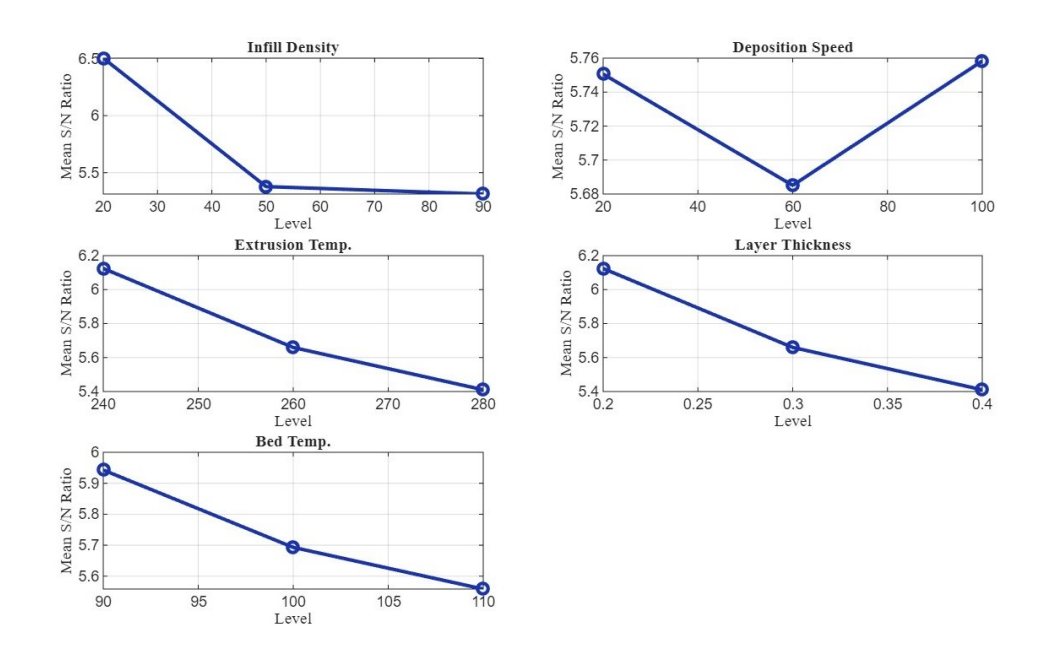


Figure 5.2: Main effects plot for total deformation S/N ratios in FFF.

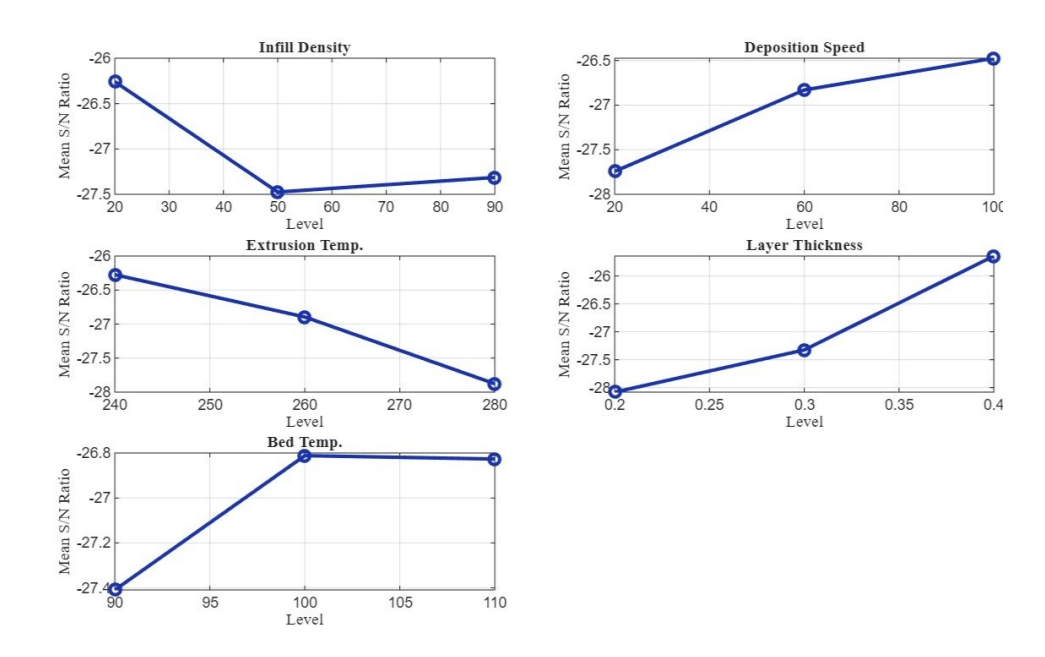


Figure 5.3: Main effects plot for residual stress S/N ratios in FFF.

5.2.4 Factor Ranking (Delta Method)

The delta method confirms the conclusions drawn based on the main effects plots and provides a clear ranking of factor importance for each response. As shown in table 5.3, extrusion temperature has the largest delta value and thus the strongest influence on warpage, followed by layer thickness. Deposition speed ranks third, while bed temperature and infill density are relatively less critical, ranking fourth and fifth,

respectively. For total deformation (table 5.4), infill density emerges as the most dominant factor, consistent with its role in governing uniform shrinkage, whereas extrusion temperature and layer thickness occupy the second and third positions. In contrast, deposition speed has minimal influence, ranking last. Finally, for residual stress (table 5.5), layer thickness is the most critical factor, followed by extrusion temperature and deposition speed, while infill density and bed temperature have the least effect. Overall, these rankings highlight that extrusion temperature and layer thickness consistently play strong roles across all responses, while bed temperature tends to be less impactful. Infill density, on the other hand, is highly influential for total deformation but comparatively unimportant for warpage and residual stress.

Table 5.3: Ranking of FFF process parameters by their influence on warpage S/N ratios

Factor	Delta	Rank
Infill Density	0.1851	5
Deposition Speed	0.3646	3
Extrusion Temp.	2.1475	1
Layer Thickness	0.5344	2
Bed Temp.	0.2045	4

Table 5.4: Ranking of FFF process parameters by their influence on total deformation S/N ratios

Factor	Delta	Rank
Infill Density	1.1910	1
Deposition Speed	0.0732	5
Extrusion Temp.	0.7142	2
Layer Thickness	0.7139	3
Bed Temp.	0.3844	4

Table 5.5: Ranking of FFF process parameters by their influence on residual stress S/N ratios

Factor	Delta	Rank
Infill Density	1.2160	4
Deposition Speed	1.2682	3
Extrusion Temp.	1.6022	2
Layer Thickness	2.4376	1
Bed Temp.	0.5972	5

5.2.5 Analysis of Variance

The analysis of variance further confirms the findings of the previous discussions. With a higher F-statistic, deposition speed, extrusion temperature, and layer thickness have a major contribution to the warpage, with respect to unexplained noise. The p-values presented in table 5.6 indicate that both extrusion temperature and layer thickness

have a statistically significant impact on the warpage of FFF parts. Deposition speed is statistically significant as well at the p < 0.05 level, with a p-value of 0.0202. In contrast, infill density and bed temperature do not show statistically significant effects on warpage within the investigated range, as their p-values exceed the conventional significance threshold of 0.05.

The relative contributions of each parameter are summarised in table 5.7. Consistent with the ranking based on the delta method, extrusion temperature is the dominant factor, accounting for 85.72% of the total variation in the warpage signal-to-noise (S/N) ratio. Layer thickness is the next most influential factor, followed by deposition speed. The low error contribution of 4.33% indicates that the experimental model effectively captures the majority of variation observed in the results.

Table 5.6: Analysis of variance for warpage S/N ratios in FFF

Source	Sum Sq.	d.f.	Mean Sq.	\mathbf{F}	Prob>F
Infill Density	0.1569	2	0.0784	1.1876	0.3304
Deposition Speed	0.6640	2	0.3320	5.0271	0.0202
Extrusion Temp.	20.8995	2	10.4498	158.2346	< 0.0001
Layer Thickness	1.3617	2	0.6808	10.3094	0.0013
Bed Temp.	0.2413	2	0.1207	1.8271	0.1929
Error	1.0566	16	0.0660		
Total	24.3800	26			

Table 5.7: Relative contribution of each FFF process parameter to warpage S/N ratios

Factor	SS	Percent Contribution
Infill Density	0.1569	0.64
Deposition Speed	0.6640	2.72
Extrusion Temp.	20.8995	85.72
Layer Thickness	1.3617	5.59
Bed Temp.	0.2413	0.99
Error	1.0566	4.33

Regarding the total deformation, tables 5.8 and 5.9 summarise the findings. In fill density, extrusion temperature, and layer thickness are the main contributors, and the error remains small. Deposition speed and bed temperature, on the other hand, do not show a strong influence.

Table 5.8: Analysis of variance for total deformation S/N ratios in FFF

Source	Sum Sq.	d.f.	Mean Sq.	\mathbf{F}	Prob>F
Infill Density	8.0727	2	4.0363	31.0755	< 0.0001
Deposition Speed	0.0291	2	0.0146	0.1122	0.8946
Extrusion Temp.	2.3654	2	1.1827	9.1057	0.0023
Layer Thickness	2.3628	2	1.1814	9.0954	0.0023
Bed Temp.	0.6851	2	0.3425	2.6372	0.1024
Error	2.0782	16	0.1299		
Total	15.5933	26			

Table 5.9: Relative contribution of each FFF process parameter to total deformation S/N ratios

Factor	SS	Percent Contribution
Infill Density	8.0727	51.77
Deposition Speed	0.0291	0.19
Extrusion Temp.	2.3654	15.17
Layer Thickness	2.3628	15.15
Bed Temp.	0.6851	4.39
Error	2.0782	13.33

The ANOVA results, reported in table 5.10, indicate that among the process parameters, layer thickness has the most significant effect on residual stress. Extrusion temperature shows a moderate influence, while infill density and deposition speed appear to have weaker, non-significant effects. Bed temperature has little to no measurable impact within the tested range.

The relative contribution analysis confirms these findings. Layer thickness emerges as the dominant factor, followed by extrusion temperature, with infill density and deposition speed playing smaller roles. Bed temperature contributes minimally. The relatively large share of unexplained variation suggests that additional factors, not considered in this study, may also influence residual stress.

Table 5.10: Analysis of variance for residual stress S/N ratios in FFF

Source	Sum Sq.	d.f.	Mean Sq.	\mathbf{F}	Prob>F
Infill Density	7.8564	2	3.9282	2.2070	0.1424
Deposition Speed	7.7024	2	3.8512	2.1638	0.1473
Extrusion Temp.	11.7461	2	5.8731	3.2998	0.0631
Layer Thickness	28.0273	2	14.0137	7.8736	0.0042
Bed Temp.	2.0869	2	1.0435	0.5863	0.5679
Error	28.4774	16	1.7798		
Total	85.8966	26			

Table 5.11: Relative contribution of each FFF process parameter to residual stress S/N ratios

Factor	SS	Percent Contribution
Infill Density	7.8564	9.15
Deposition Speed	7.7024	8.97
Extrusion Temp.	11.7461	13.67
Layer Thickness	28.0273	32.63
Bed Temp.	2.0869	2.43
Error	28.4774	33.15

5.2.6 Probability Plots

Figures 5.5 and 5.6 confirm that the results for total deformation and residual stress follow normal distributions. In the case of warpage, however, the results corresponding to runs 1, 7, 15, 20, and 24 are considered anomalies, as they fall outside the 95% confidence boundaries. The associated p-value is below 0.05, indicating that the null hypothesis of normality must be rejected. This suggests that the warpage data deviate significantly from a normal distribution, and the corresponding analysis should therefore be interpreted with caution.

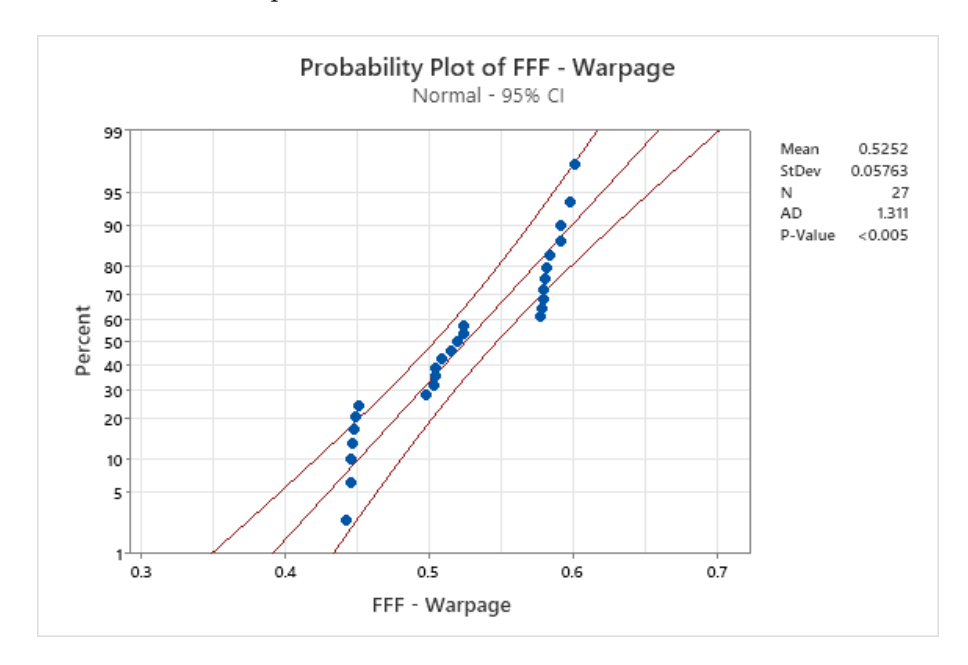


Figure 5.4: Probability plot for warpage in FFF (pre-annealing).

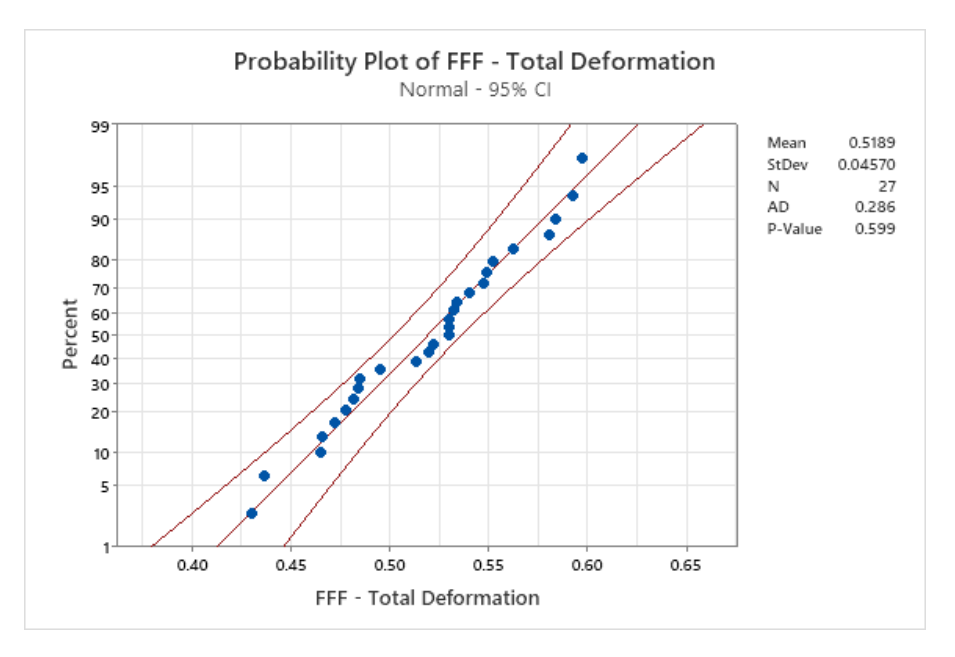


Figure 5.5: Probability plot for total deformation in FFF (pre-annealing).

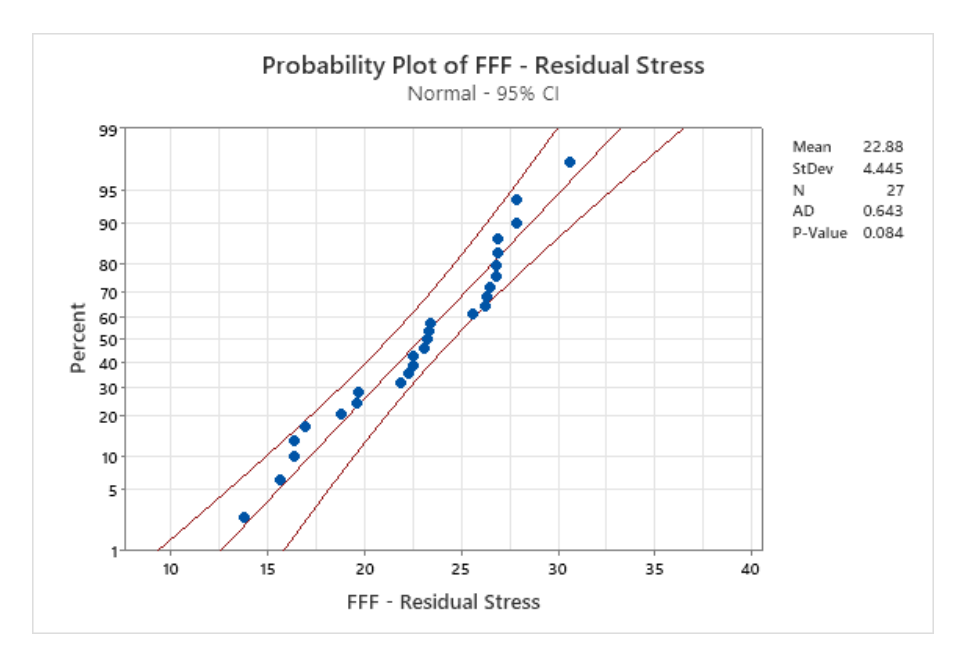


Figure 5.6: Probability plot for residual stress in FFF (pre-annealing).

5.2.7 Optimal Parameter Levels

The optimal parameter levels identified through the Taguchi analysis and corresponding main effects plots are summarised in tables 5.12 and 5.13. For warpage and total deformation, the most robust combination consists of low infill density, moderate deposition speed, high extrusion temperature, medium layer thickness, and elevated bed temperature. In contrast, minimising residual stress requires similar settings for most parameters, with the main differences being a thicker layer and slightly higher bed temperature. Since the primary objective of this study is to reduce total deformation, the parameter levels optimised for this response will be adopted in

the subsequent simulations and discussions. This ensures that the selected process settings prioritise dimensional accuracy and geometric stability of the printed parts.

Table 5.12: Most robust parameter levels to minimise warpage and total deformation in FFF

Parameter	Level
Infill Density	20 %
Deposition Speed	$100~{\rm mm}{\rm s}^{-1}$
Extrusion Temp.	240 °C
Layer Thickness	$0.2 \mathrm{mm}$
Bed Temp.	90 °C

Table 5.13: Most robust parameter levels to minimise residual stress in FFF

Parameter	Level
Infill Density	20 %
Deposition Speed	$100 \mathrm{mm s^{-1}}$
Extrusion Temp.	240 °C
Layer Thickness	$0.4 \mathrm{mm}$
Bed Temp.	100 °C

5.2.8 Confirmation of the Optimal Settings

Table 5.12 reports the selected settings for the FFF process to minimize deformation. In this case, the Taguchi analysis identified a parameter combination that was not directly tested in the DOE. Therefore, a confirmation test was conducted to validate the prediction. The results of this test are compared in Table 5.14 against Run 9, which exhibited the lowest total deformation, and Run 19, which had the lowest warpage in the conducted experiments. The confirmation test demonstrates that the parameters suggested by the Taguchi method indeed yield the lowest warpage and achieve a total deformation value very close to the minimum observed, while also reducing residual stress significantly. This outcome confirms the effectiveness and robustness of the optimisation approach. These process parameters will be the base for carrying out annealing and geometry compensation.

Table 5.14: Confirmation of the optimal process parameters for FFF

Run	Warpage (mm)	$\begin{array}{c} \text{Total} \\ \text{deformation} \\ \text{(mm)} \end{array}$	Stress (MPa)
9	0.5810	0.4297	27.39
19	0.4458	0.4779	27.34
Confirmation Test	0.4396	0.4400	23.77

5.3 SLS Simulation Results

5.3.1 Raw Simulation Results

Table 5.15 summarises the maximum values of warpage, total deformation, and stress obtained from the 25 simulation runs carried out in the selective laser sintering study, based on the DOE outlined in table 4.7. As opposed to the FFF process, since an

elevated chamber temperature is used in the SLS process, the values of residual stress are much lower. Likewise, SLS also offers lower warpage, while the total deformation is higher due to the material shrinkage. These results provide the basis for the statistical analysis of how process parameters influence part performance, which will be discussed in the following section.

Table 5.15: Simulation results for SLS (pre-annealing)

Run	Warpage	Total	Stress
	(mm)	$rac{ ext{deformation}}{ ext{(mm)}}$	(MPa)
		(111111)	
1	0.2621	0.6106	4.730
2	0.2654	0.6267	3.357
3	0.2678	0.6313	3.288
4	0.2697	0.6477	3.166
5	0.2713	0.6656	3.304
6	0.2671	0.6267	3.437
7	0.2690	0.6324	3.265
8	0.2703	0.6424	3.104
9	0.2722	0.6656	3.309
10	0.2729	0.6685	3.198
11	0.2704	0.6323	3.075
12	0.2716	0.6357	3.344
13	0.2738	0.6651	3.452
14	0.2755	0.6681	3.452
15	0.2774	0.6664	3.450
16	0.2742	0.6319	3.058
17	0.2772	0.6642	3.344
18	0.2792	0.6654	3.323
19	0.2814	0.6603	3.088
20	0.2835	0.6533	3.713
21	0.2825	0.6488	3.615
22	0.2865	0.6335	2.170
23	0.2897	0.6207	1.951
24	0.2921	0.6123	1.833
25	0.2938	0.6071	1.776

5.3.2 Signal-to-Noise Ratio Computation

As expected, S/N ratios reported in table 5.16 indicate low warpage, and the residual stresses are smaller with respect to the FFF process. Total deformation, however, is less favourable. This is due to volumetric shrinkage, which is easy to compensate for.

Table 5.16: Signal-to-noise ratios for SLS simulation results

Run	Warpage S/N (dB)	Total Deformation	Residual Stress
		S/N (dB)	S/N (dB)
1	11.6307	4.2849	-13.4972
2	11.5220	4.0588	-10.5190
3	11.4438	3.9953	-10.3386
4	11.3824	3.7725	-10.0102
5	11.3310	3.5357	-10.3808
6	11.4665	4.0588	-10.7236
7	11.4050	3.9802	-10.2777
8	11.3631	3.8439	-9.8384
9	11.3022	3.5357	-10.3939
10	11.2799	3.4980	-10.6372
11	11.3599	3.9815	-10.0976
12	11.3214	3.9350	-9.7569
13	11.2513	3.5423	-10.4853
14	11.1976	3.5032	-10.7614
15	11.1379	3.5253	-10.7614
16	11.2387	3.9870	-9.7087
17	11.1441	3.5540	-10.4853
18	11.0817	3.5383	-10.4306
19	11.0135	3.6052	-9.7935
20	10.9489	3.6977	-8.6690
21	10.9796	3.7578	-8.3494
22	10.8575	3.9651	-6.7292
23	10.7610	4.1424	-5.8051
24	10.6894	4.2607	-5.2632
25	10.6390	4.3348	-4.9889

5.3.3 Main Effects Plots

The main effects plot for warpage in SLS, shown in figure 5.7, highlights the influence of key process parameters on dimensional stability. Lower temperatures reduce warpage by limiting thermal expansion of the powder and minimising uneven cooling, whereas excessively high chamber temperatures can increase warpage due to additional energy absorption by the powder, which amplifies thermal gradients. The steep slope observed for chamber temperature in the main effects plot indicates its strong sensitivity, confirming that careful control of preheating is critical to achieving minimal distortion in SLS parts.

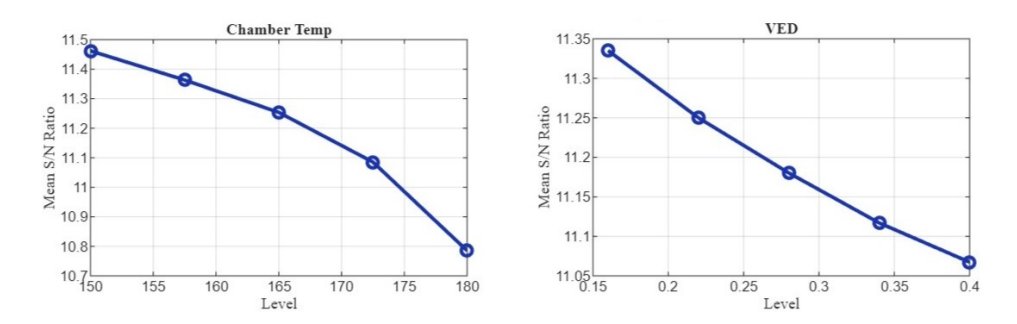


Figure 5.7: Main effects plot for warpage S/N ratios in SLS.

Considering the total deformation, the effect of VED is similar to warpage. However, a sudden increase in the S/N ratio is interesting when the chamber temperature is increased from 172.5 to 180 °C.

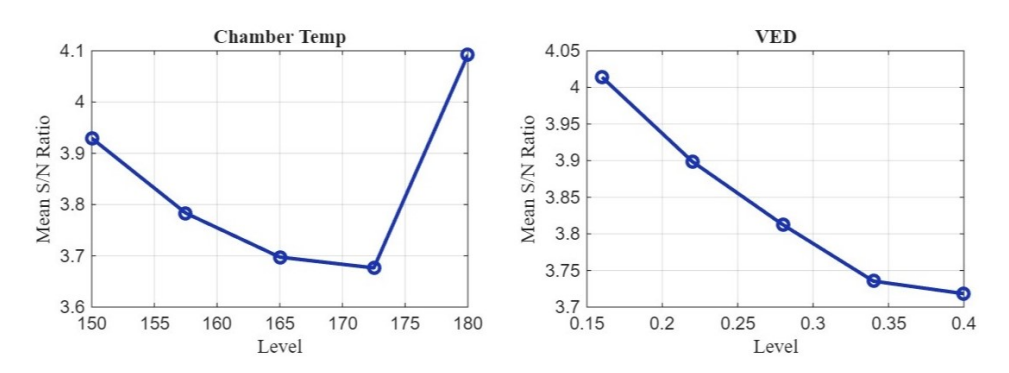


Figure 5.8: Main effects plot for total deformation S/N ratios in SLS.

Considering residual stress, increasing the chamber temperature to 180 °C results in a sharp improvement, again. Interestingly, the effect of VED is reversed compared to total deformation, with higher VEDs now contributing to reduced residual stress. In this case, the sensitivity to chamber temperature is much higher.

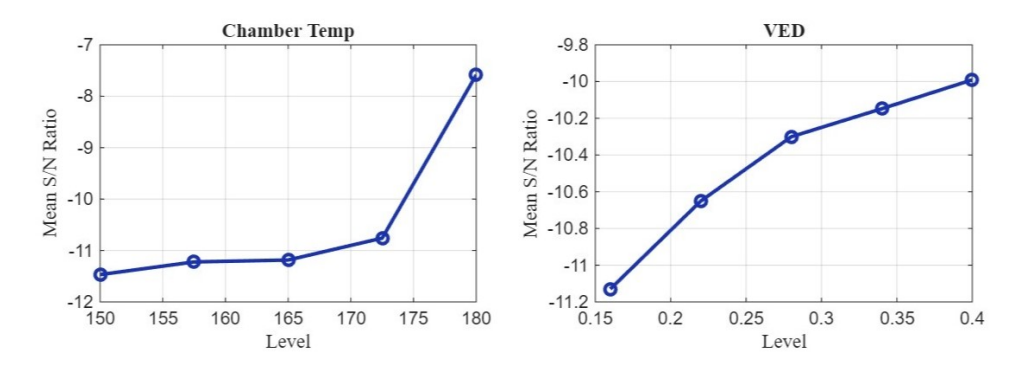


Figure 5.9: Main effects plot for residual stress S/N ratios in SLS.

The three main contributors to warpage are also the primary contributors to residual stress, which is consistent since both phenomena arise from uneven cooling. Lower infill densities and extrusion temperatures help reduce both warpage and residual stress, while a higher deposition speed is generally preferable. However,

although a lower layer thickness is beneficial for minimising warpage and total deformation, it can have a detrimental effect by increasing residual stresses. This occurs because thinner layers cool and solidify more quickly, which traps internal strains before they can relax, leading to higher residual stresses. Figure 5.3 illustrates these trends in the main effects plots, highlighting how each parameter influences residual stress.

5.3.4 Factor Ranking (Delta Method)

The delta values confirm that chamber temperature is the dominant parameter influencing both warpage and total deformation, while the volumetric energy density has a comparatively smaller effect. The difference in delta magnitudes highlights that the system is more sensitive to changes in chamber temperature, which directly affects the thermal gradients and cooling rates during printing. In contrast, VED plays a secondary role by influencing the local melting and bonding of particles, but with less impact on the overall dimensional stability. These results are consistent across both responses, reinforcing chamber temperature as the most critical factor in controlling distortion in SLS.

Table 5.17: Ranking of SLS process parameters by their influence on warpage S/N ratios

Factor	Delta	Rank
Chamber Temp	0.6767	1
VED	0.2677	2

Table 5.18: Ranking of SLS process parameters by their influence on total deformation S/N ratios

Factor	Delta	Rank
Chamber Temp	0.4157	1
VED	0.2957	2

Table 5.19: Ranking of SLS process parameters by their influence on residual stress S/N ratios

Factor	Delta	Rank
Chamber Temp	4.7220	1
VED	1.3879	2

5.3.5 Analysis of Variance

The results of the ANOVA for the SLS simulations are presented in tables 5.20–5.24, together with the relative contributions in tables 5.25–5.23. For warpage, both chamber temperature and volumetric energy density (VED) are statistically significant, with chamber temperature clearly dominating the response. This is

reflected in its high contribution to the variation in the signal-to-noise ratio, while VED accounts for a much smaller share.

Residual stress is also strongly influenced by chamber temperature, which contributes the vast majority of the observed variation. In contrast, VED shows no statistically significant effect. These findings highlight the strong sensitivity of residual stress to thermal boundary conditions within the build chamber.

For total deformation, however, neither chamber temperature nor VED reached statistical significance at the 95% confidence level. This is further supported by the large proportion of unexplained variation attributed to error, suggesting that other factors not included in the present design may play a more important role in driving overall deformation.

Taken together, the ANOVA results emphasise chamber temperature as the most critical factor for both warpage and residual stress, whereas total deformation appears to depend on additional influences beyond those captured by the chosen parameters.

Table 5.20: Analysis of variance for warpage S/N ratios in SLS

Source	Sum Sq.	d.f.	Mean Sq.	\mathbf{F}	Prob>F
Chamber Temp	1.4139	4	0.3535	526.8865	< 0.0001
VED	0.2256	4	0.0564	84.0533	< 0.0001
Error	0.0107	16	0.0007		
Total	1.6502	24			

Table 5.21: Relative contribution of each SLS process parameter to warpage S/N ratios

Factor	SS	Percent Contribution
Chamber Temp	1.4139	85.68
VED	0.2256	13.67
Error	0.0107	0.65

Table 5.22: Analysis of variance for total deformation S/N ratios in SLS

Source	Sum Sq.	d.f.	Mean Sq.	\mathbf{F}	Prob > F
Chamber Temp	0.6088	4	0.1522	2.7997	0.0616
VED	0.3006	4	0.0751	1.3823	0.2843
Error	0.8699	16	0.0544		
Total	1.7793	24			

Table 5.23: Relative contribution of each SLS process parameter to total deformation S/N ratios

Factor SS		Percent Contribution
Chamber Temp	0.6088	34.22
VED	0.3006	16.89
Error	0.8699	48.89

Table 5.24: Analysis of variance for residual stress S/N ratios in SLS

Source	Sum Sq.	d.f.	Mean Sq.	\mathbf{F}	Prob>F
Chamber Temp	72.1309	4	18.0327	22.02	< 0.0001
VED	5.9626	4	1.4906	1.8170	0.1742
Error	13.1003	16	0.8188		
Total	91.1938	24			

Table 5.25: Relative contribution of each SLS process parameter to residual stress S/N ratios

Factor	SS	Percent Contribution
Chamber Temp	72.131	79.10
VED	5.9626	6.54
Error	13.1	14.37

5.3.6 Probability Plots

Figures 5.10–5.12 present the probability plots obtained from the SLS simulation results. The plots for warpage and total deformation align closely with the normal distribution line, indicating that these responses can be reasonably modelled by a normal distribution. In contrast, the residual stress data exhibit noticeable deviations from normality, with a p-value below the 0.005 significance threshold. This suggests that residual stress is influenced by factors that introduce non-normal variability, which may need to be accounted for in further modelling or process optimisation.

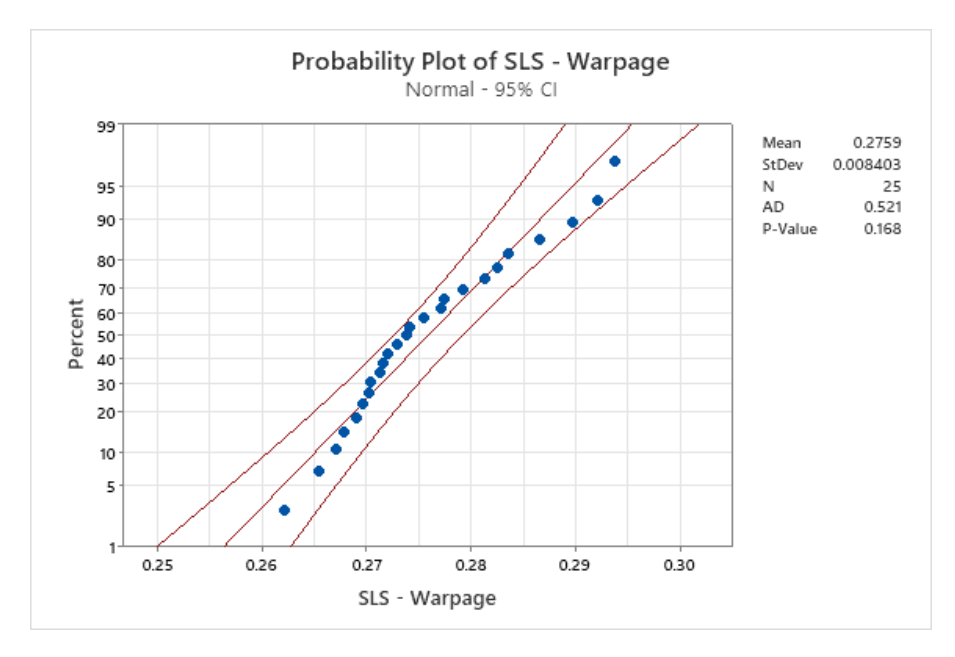


Figure 5.10: Probability plot for warpage in SLS

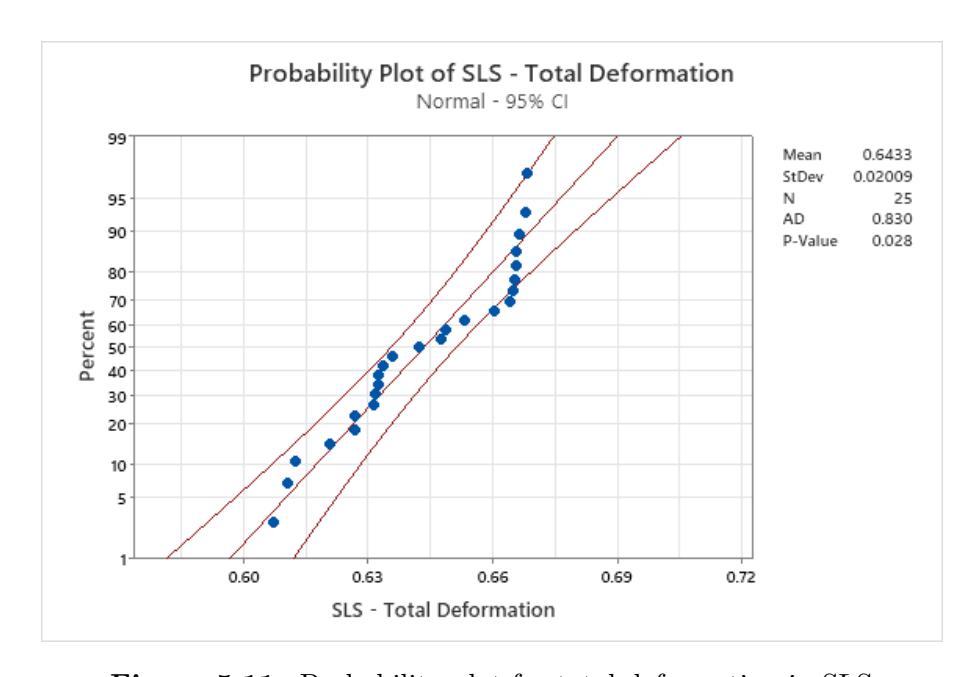


Figure 5.11: Probability plot for total deformation in SLS

The probability plot for residual stress (figure 5.12) indicates that the data does not follow a normal distribution, as the points deviate noticeably from the reference line. This behaviour is reasonable, since the elevated chamber temperatures in the SLS process promote stress relief up to a certain limit, resulting in most of the data clustering within the range of 3 to 3.5 MPa.

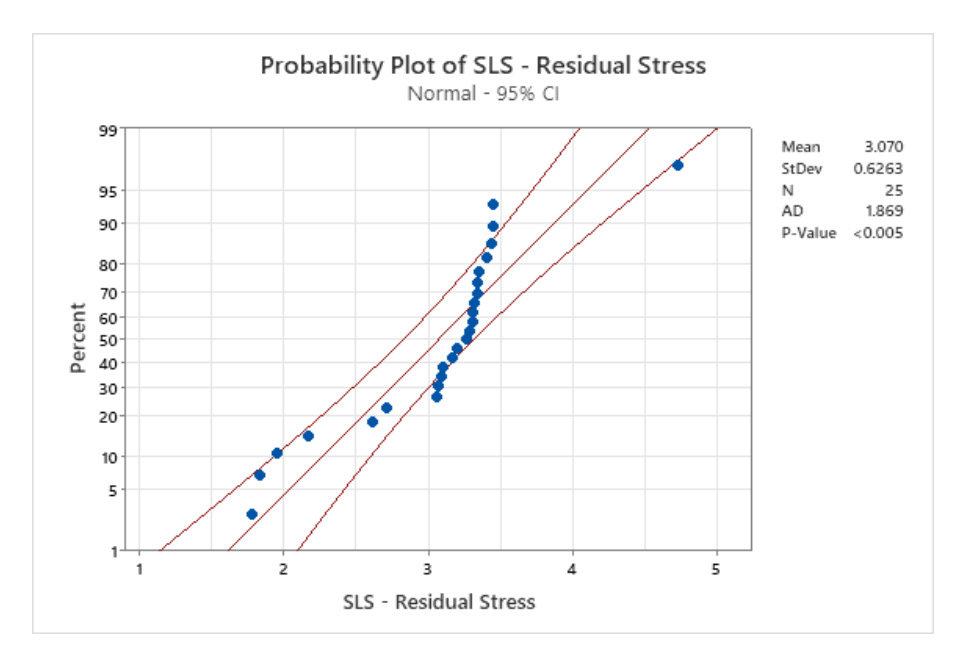


Figure 5.12: Probability plot for residual stress in SLS

5.3.7 Optimal Parameter Levels

The optimal parameter levels for warpage, total deformation, and residual stress are summarised in tables 5.26–5.28. While each response has slightly different optimal settings, the primary objective of this study is to minimise total deformation. Therefore, the chamber temperature and VED levels identified for total deformation will be adopted in the subsequent analyses to ensure dimensional accuracy and geometric stability of the printed parts.

Table 5.26: Most robust parameter levels to minimise warpage in SLS

Parameter	Level
Chamber Temp.	150 °C
VED	$0.16~{ m J}{ m mm}^{-2}$

Table 5.27: Most robust parameter levels to minimise total deformation in SLS

Parameter	Level
Chamber Temp.	180 °C
VED	$0.16~{ m J}{ m mm}^{-2}$

Table 5.28: Most robust parameter levels to minimise residual stress in SLS

Parameter	Level
Chamber Temp.	180 °C
VED	$0.40~{ m J}{ m mm}^{-2}$

5.3.8 Confirmation of the Optimal Settings

Tables 5.27 reports the final process parameters used for the SLS process. The chosen parameter set corresponds to Run 21. In this case, the chosen parameters do not directly yield the lowest deformation. However, are the most robust settings, leading to the minimum unexplained variations according to the methodology.

Chapter 6

Residual Stress and Deformation Mitigation

While the spur gear produced by the SLS process exhibits acceptable levels of residual stress, the one manufactured by FFF requires an additional annealing step before it's suitable for use. Therefore, at this stage, annealing is applied exclusively to the FFF part to reduce the residual von Mises stress to levels comparable to those of the SLS counterparts. As outlined in Chapters 3 and 4, the annealing trials explored durations ranging from 3 to 18 hours and temperatures between $135\,^{\circ}\mathrm{C}$ and $165\,^{\circ}\mathrm{C}$. These ranges were selected based on findings from the literature review on PA12 material.

6.1 Annealing Simulation Results

Based on the DOE presented in table 4.8, the simulations are carried on on the basis of the FFF parameters tuned by the Taguchi method. The results of the annealing simulations are summarised in this section. Data on warpage, total deformation, and residual stress are collected for each run. This provides a baseline for understanding the influence of annealing parameters before applying any geometry compensation.

The results show an immediate reduction in the value of residual von Mises stress even with the lowest temperature and duration. Total deformation of the part increases; however, there's a reduction in warpage with low temperatures. As the temperature increases, the deformations increase, and the stress is released.

Table 6.1: Simulation results for FFF (post-annealing)

Run	Warpage (mm)	Total deformation (mm)	Stress (MPa)
Base	0.4396	0.4400	23.77
1	0.3083	0.6233	10.99
2	0.3100	0.6293	10.45
3	0.3123	0.6369	9.856
4	0.3140	0.6421	9.474

	1	c		
	continued	from	previous	page

Run	Warpage (mm)	Total deformation (mm)	Stress (MPa)
5	0.3344	0.6920	6.857
6	0.3465	0.7158	6.022
7	0.3643	0.7469	5.171
8	0.3779	0.7687	4.913
9	0.4625	0.8848	4.780
10	0.4625	0.8848	4.780
11	0.4623	0.8848	4.780
12	0.4622	0.8848	4.780

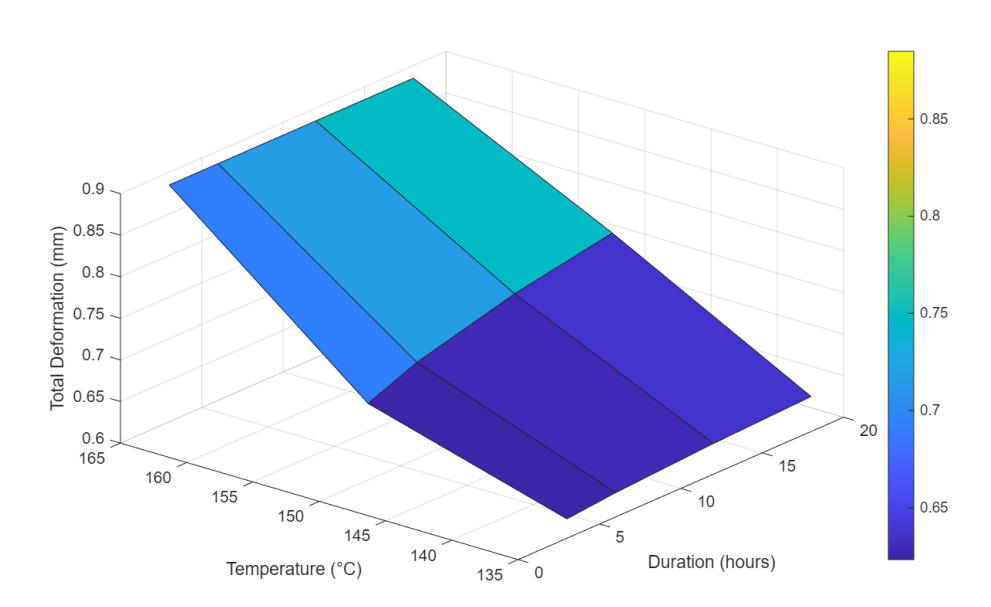


Figure 6.1: Surface plot showing total deformation of annealed samples

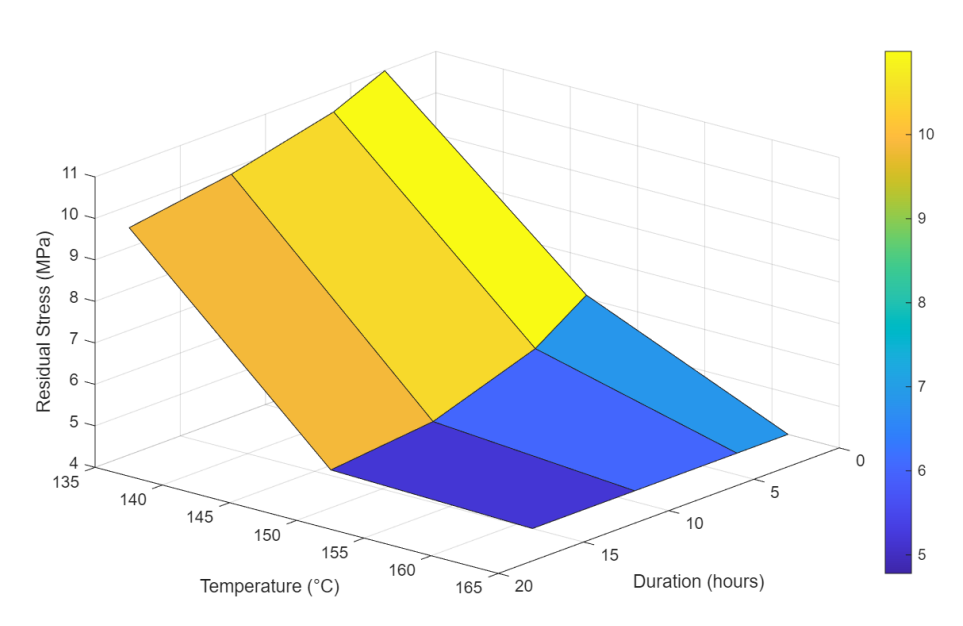


Figure 6.2: Surface plot showing residual stress in annealed samples

6.2 Statistical Analysis of Annealing Parameters

The results of the annealing experiments reveal a clear and consistent trend. Higher annealing temperatures and longer durations result in increased shrinkage and deformation, while simultaneously reducing residual stress. Given this straightforward relationship, a full statistical analysis and Taguchi-based optimisation are unnecessary, as the methodology would trivially suggest Run 1 for minimising shape deviations and Run 12 for minimising residual stress. Instead, a trade-off approach is adopted to balance the reduction of residual stress against the need to limit excessive dimensional changes.

6.2.1 Signal-to-Noise Ratio Computation

Table 6.2 presents the signal-to-noise ratios calculated from the annealing simulation results. The S/N ratios, computed using the *smaller-the-better* criterion, quantify the robustness of each run with respect to warpage, total deformation, and residual stress. Higher S/N values indicate more desirable and consistent outcomes. From the table, it can be observed that lower annealing temperatures and shorter durations tend to yield higher S/N ratios for dimensional accuracy, while higher temperatures favour residual stress reduction. This information forms the basis for assessing trade-offs in selecting optimal annealing parameters.

Table 6.2: Signal-to-noise ratios for annealing simulation results

Run	Warpage S/N (dB)	Total Deformation S/N (dB)	Residual Stress S/N (dB)
1	10.2205	4.1061	-20.8200
2	10.1728	4.0228	-20.3823
3	10.1086	3.9186	-19.8740
4	10.0614	3.8479	-19.5307
5	9.5147	3.1979	-16.7227
6	9.2059	2.9042	-15.5948
7	8.7708	2.5348	-14.2715
8	8.4525	2.2849	-13.8269
9	6.6978	1.0631	-13.5886
10	6.6978	1.0631	-13.5886
11	6.7015	1.0631	-13.5886
12	6.7034	1.0631	-13.5886

6.2.2 Analysis of Variance

The ANOVA results in Tables 6.3–6.5 indicate that the main effect in all three responses comes predominantly from the annealing temperature. The contribution

of duration is comparatively small, and the residual error is minimal, confirming the consistency of the simulations. Given the clear dominance of temperature, there is no need to apply the delta method for ranking factor influence, as the results are already straightforward and unambiguous.

Table 6.3: Analysis of variance for warpage S/N ratios in FFF post-annealing

Source	Sum Sq.	d.f.	Mean Sq.	F	Prob>F
Temperature	24.5297	2	12.2648	190.4852	< 0.0001
Duration	0.2873	3	0.0958	1.4871	0.3101
Error	0.3863	6	0.0644		
Total	25.2032	11			

Table 6.4: Analysis of variance for total deformation S/N ratios in FFF post-annealing

Source	Sum Sq.	d.f.	Mean Sq.	\mathbf{F}	Prob>F
Temperature	17.0648	2	8.5324	198.3910	< 0.0001
Duration	0.2663	3	0.0888	2.0636	0.2066
Error	0.2580	6	0.0430		
Total	17.5891	11			

Table 6.5: Analysis of variance for residual stress S/N ratios in FFF post-annealing

Source	Sum Sq.	d.f.	Mean Sq.	\mathbf{F}	Prob>F
Temperature	94.4690	2	47.2345	108.2152	< 0.0001
Duration	3.5286	3	1.1762	2.6947	0.1393
Error	2.6189	6	0.4365		
Total	100.6165	11			

6.3 Selection of Annealing Settings

Instead of selecting a single optimal setting, a trade-off between deformation and residual stress is considered. Figures 6.1 and 6.2 show surface plots of deformation and residual stress as functions of annealing temperature and duration. These plots illustrate that increasing the temperature by one level causes a sharp rise in deformation while significantly reducing residual stress. In contrast, at a constant temperature, extending the annealing duration results in more gradual changes in both responses. Based on this analysis, Run 7 was selected as a trade-off, as it reduces residual stress to nearly 5 MPa while keeping the maximum deformation around 0.16 mm lower than annealing at 165 °C.

6.4 Overview of Geometry Compensation

A brief overview of the geometry compensation workflow was provided in subsection 3.1.1. Here, the practical steps involved in this workflow are described in more detail.

During simulation setup, the part geometry is imported as an STL file. This representation provides a tessellated surface mesh of the part. The software then generates a voxel mesh to perform the finite element simulation. After performing the base simulation using the selected printing process parameters and annealing specifications, the post-processing module of the software displays the obtained results. These results can be visualised either on the voxel mesh or mapped back onto the tessellated mesh, allowing the contours to be displayed directly on the part geometry. It is important to note that if the tessellation mesh is not sufficiently refined, the displayed results may differ from those obtained on the voxel mesh. Mesh refinement becomes particularly critical for complex geometries, such as the studied helical gear.

Once the simulation is complete, the reference and warped geometries can be exported using the tessellated mesh. The compensated geometry can also be exported as an STL file. These geometries can then be fed back into the software to perform subsequent simulations. In these simulations, deformation is calculated with respect to the reference geometry rather than the compensated geometry, based on which the part will be manufactured.

For Fused Filament Fabrication, a new tool path must be generated to match the compensated geometry. The warped geometry can be inspected in CAD software, such as Autodesk Inventor. The cycle of generating compensated geometry, simulating, and inspecting can be repeated iteratively until no further improvement in dimensional accuracy is observed.

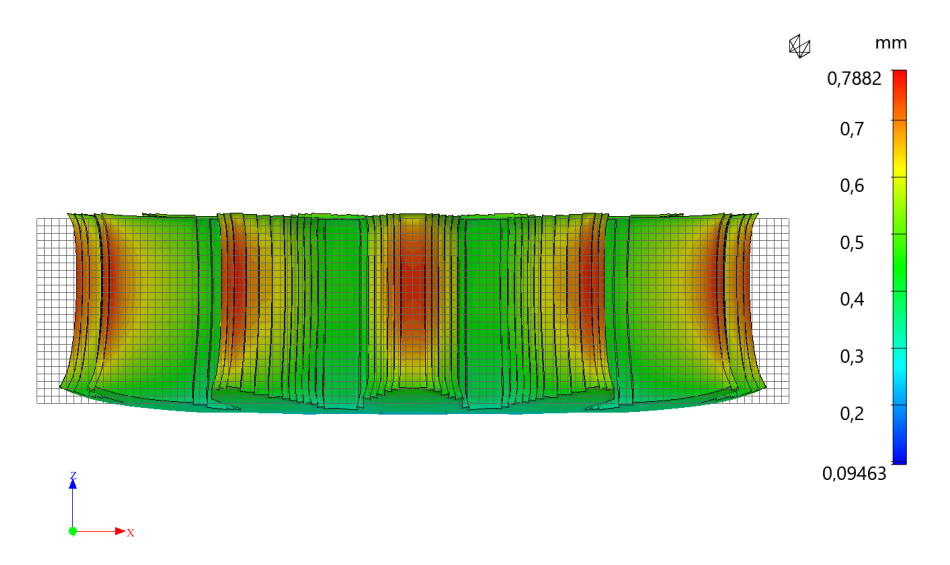


Figure 6.3: Exaggerated visualisation of deformation of the annealed FFF part

Figure 6.3 shows the deformed voxelized mesh of the spur gear overlapped by the original one, for the FFF process after annealing. The deformation is exaggerated with a scale factor of 3 for clarity. As is typical of polymer FFF parts, the edges of the component lift upward from the build platform. The volumetric shrinkage of the part is evident when compared with the original voxelized mesh. It can also be observed that the vertical edges of the part, specifically the top land of the gear teeth, exhibit a concave curvature.



Figure 6.4: Compensated geometry from FFF simulations

Figure 6.4 illustrates the final compensated geometry obtained from the FFF simulations. The STL file is rendered in Autodesk Inventor, with two dark flat plates included to highlight the surface curvatures. The compensated geometry incorporates concave curvatures on the bottom surface, counteracting the upward curvature observed at the part edges. The vertical edges, in turn, display a convex curvature, compensating for the inward shrinkage of the top land of the gear teeth. Additionally, the part is uniformly scaled to account for overall volumetric shrinkage.

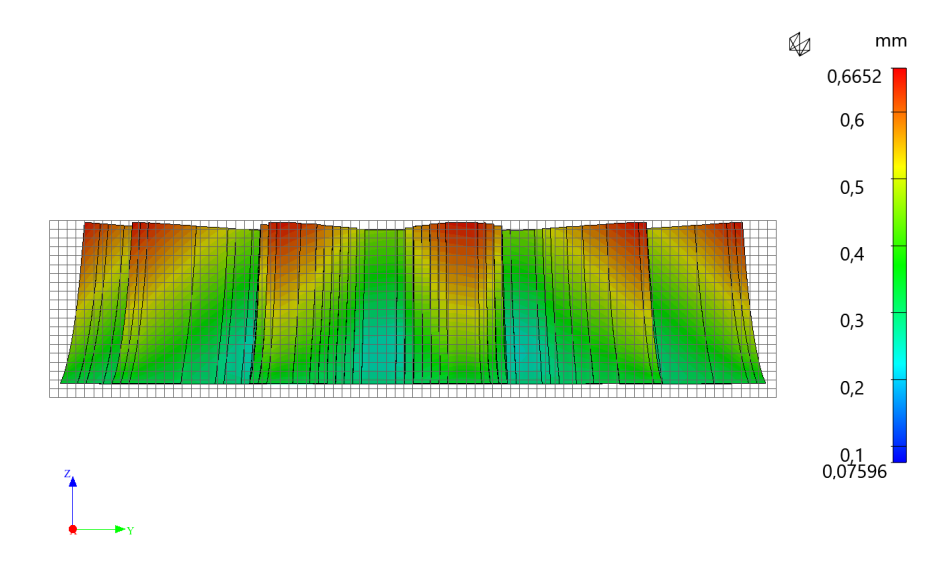


Figure 6.5: Exaggerated visualisation of deformation in SLS part

Figure 6.5 shows the exaggerated deformation in the SLS part printed using the optimised parameters. While the maximum deformation is of the same order of magnitude as in the FFF part, the deformation pattern differs significantly. In contrast to the FFF process, the bottom layers of the SLS print remain relatively flat, while the upper layers experience the greatest shrinkage. The edges of the part exhibit smoother curvatures compared to FFF, with less pronounced upward lifting.

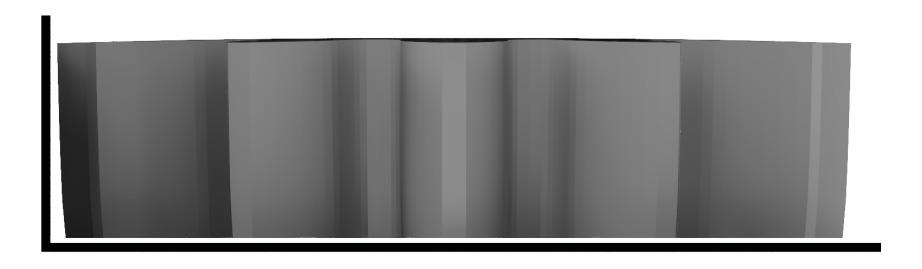


Figure 6.6: Compensated geometry from SLS simulations

Figure 6.6 depicts the STL file of the compensated geometry generated for the final compensation cycle in SLS. The model is displayed in Autodesk Inventor, with two flat reference planes added to highlight the adjusted curvatures of the geometry. The compensation introduces a convex face on top, and the top edges of the teeth are expanded outward to battle the shrinkage.

6.5 Implementation of the Geometry Compensation Cycles

The compensation cycles were implemented following the workflow described before, using the same process and simulation settings outlined in Chapters 3 and 4. As expected, the compensated geometry does not influence the residual stresses or absolute warpage of the part; instead, it alters the total deformation measured relative to the as-designed geometry. Table 6.6 summarises the maximum deviation from the reference geometry for each cycle, compared with the base simulation. The base simulation corresponds to the process parameters optimised using the Taguchi method.

For the part manufactured using the FFF process, the results of total deviation from the intended design are shown in Figures 6.7 and 6.8. The results illustrate how the software progressively reduces deformation through successive compensation cycles. However, a single cycle is insufficient to achieve the desired dimensional quality, and additional simulations are required. Furthermore, the deviation from the intended shape does not converge to zero; after a few cycles, the improvement becomes negligible.

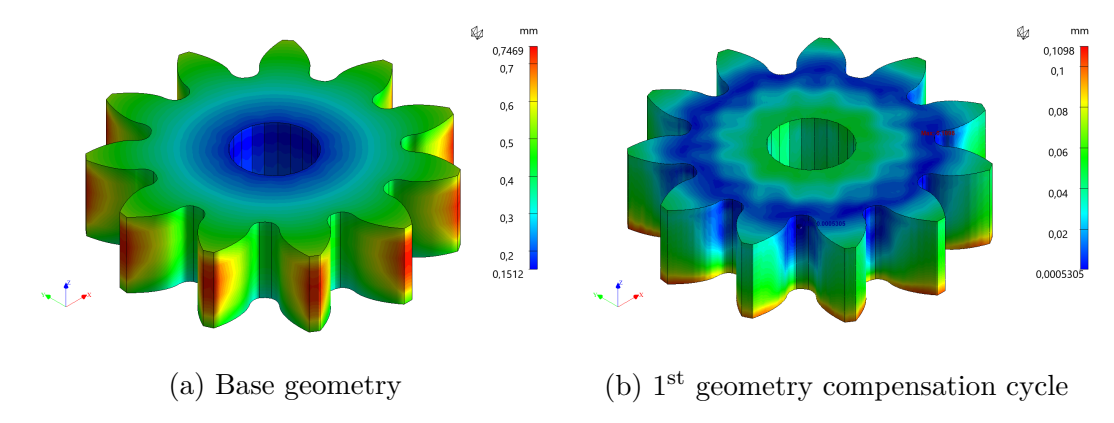


Figure 6.7: Effect of compensated geometries of deformation reduction in FFF spur gear

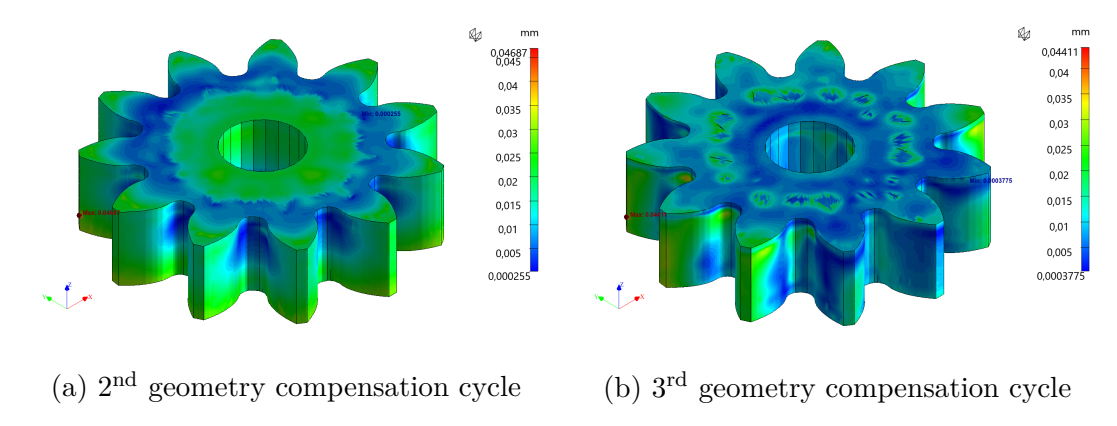


Figure 6.8: Effect of compensated geometries of deformation reduction in FFF spur gear

Table 6.6: Maximum deviation from the reference geometry in the annealed spur gear after successive compensation cycles in the FFF process

Run	Maximum Deviation
Base	$0.7496\mathrm{mm}$
Cycle 1	$0.1098\mathrm{mm}$
Cycle 2	$0.04687\mathrm{mm}$
Cycle 3	$0.04265\mathrm{mm}$

Figure 6.9 illustrates the reduction in shape deviation for the SLS-printed parts. A lower maximum deformation is achieved compared to the FFF process, and convergence is reached within fewer compensation cycles. Moreover, the deformation of the gear teeth is noticeably more uniform than in the FFF case, where the contours are significantly more complex. Since ISO standards emphasise the measurement of tooth flank deviation, this improvement in uniformity is expected to have a positive impact on the overall dimensional quality of the part.

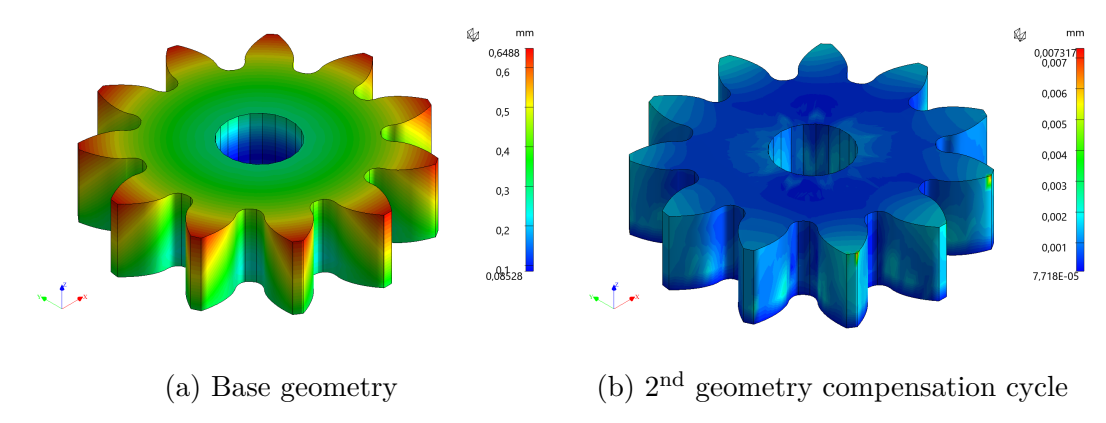


Figure 6.9: Effect of compensated geometries of deformation reduction in SLS spur gear

Table 6.7: Maximum deviation from the reference geometry in the spur gear after successive compensation cycles in the sls process

Run	Maximum Deviation
Base	$0.6488\mathrm{mm}$
Cycle 1	$0.06315\mathrm{mm}$
Cycle 2	$0.007317\mathrm{mm}$

6.6 Evaluation of Compensation Effectiveness

Figure 6.10 compares the deformed shapes obtained using the base and compensated geometries for the FFF process. As expected, the maximum total deformation relative to the initial voxelized mesh remains the same in both cases, while the compensated geometry results in a final shape with noticeably flatter edges. The difference is particularly evident along the side surfaces, and the bottom face of the compensated part exhibits less upward lifting compared to the base geometry.

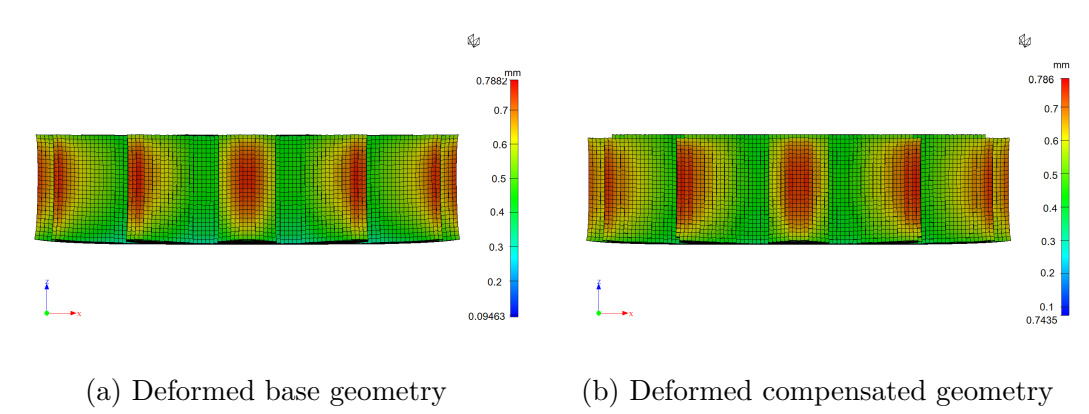
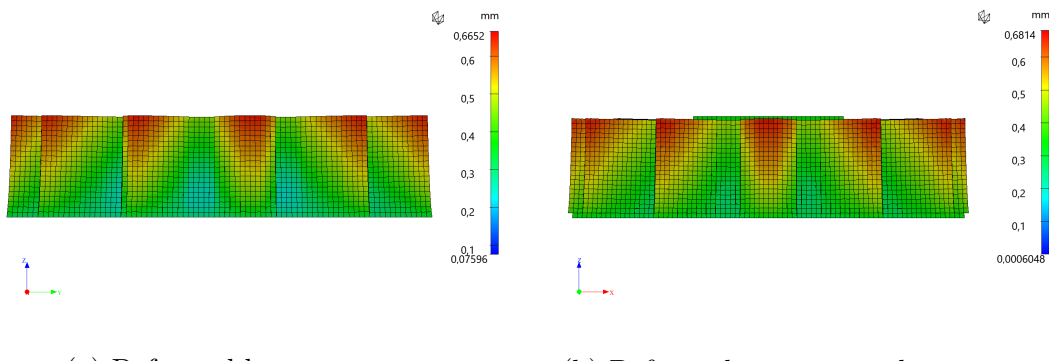


Figure 6.10: Comparison of deformed meshes between the base geometry and the compensated geometry for the FFF process

Figure 6.11 shows a similar comparison for the SLS process. Again, the maximum total deformation relative to the voxelized mesh is unchanged. However, the com-

pensated geometry exhibits flatter edges and improved overall dimensional stability compared to the base geometry.



- (a) Deformed base geometry
- (b) Deformed compensated geometry

Figure 6.11: Comparison of deformed meshes between the base geometry and the compensated geometry for the SLS process

6.7 Extension to Large Helical Gear

For the helical gear, the simulations are carried out with the same printing process and annealing parameters tuned in the previous sections. In the part printed with the SLS technology, however, residual stresses exist above the acceptable level. Therefore, both parts are annealed with the parameters fixed before.

Regarding the helical gear obtained by the FFF process, figures 6.12 and 6.13 display the improvement in geometrical accuracy as compensation cycles are carried out. However, the maximum deformation stays at around 100 μm , without significant improvement after the $3^{\rm rd}$ geometry compensation cycle.

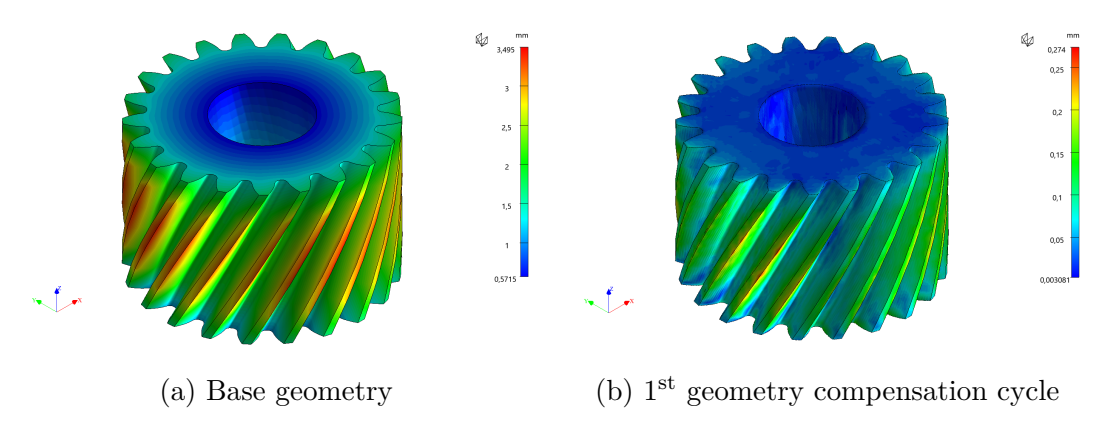


Figure 6.12: Effect of compensated geometries of deformation reduction in FFF helical gear

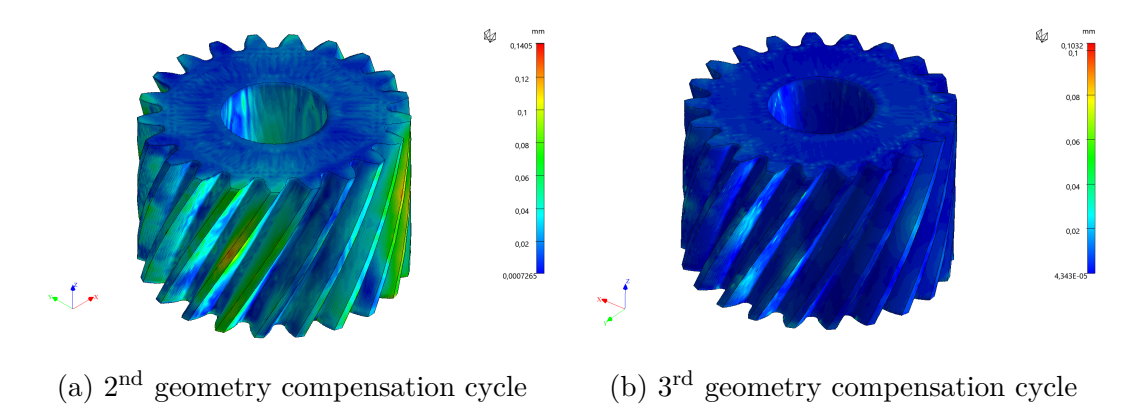


Figure 6.13: Effect of compensated geometries of deformation reduction in FFF helical gear

Table 6.8 reports the maximum deviation recorded after each simulation. It is evident that no significant improvement is achieved after the 3rd geometry compensation cycle. While the deformation is mostly uniform on the final part shown in figure 6.13(b), bright spots seen on the teeth present an issue.

Table 6.8: Maximum deviation from the reference geometry in the annealed helical gear after successive compensation cycles in the FFF process

Run	Maximum Deviation
Base	$3.495\mathrm{mm}$
Cycle 1	$0.2740\mathrm{mm}$
Cycle 2	$0.1405\mathrm{mm}$
Cycle 3	$0.1032\mathrm{mm}$
Cycle 4	$0.09737\mathrm{mm}$
Cycle 5	$0.09970\mathrm{mm}$

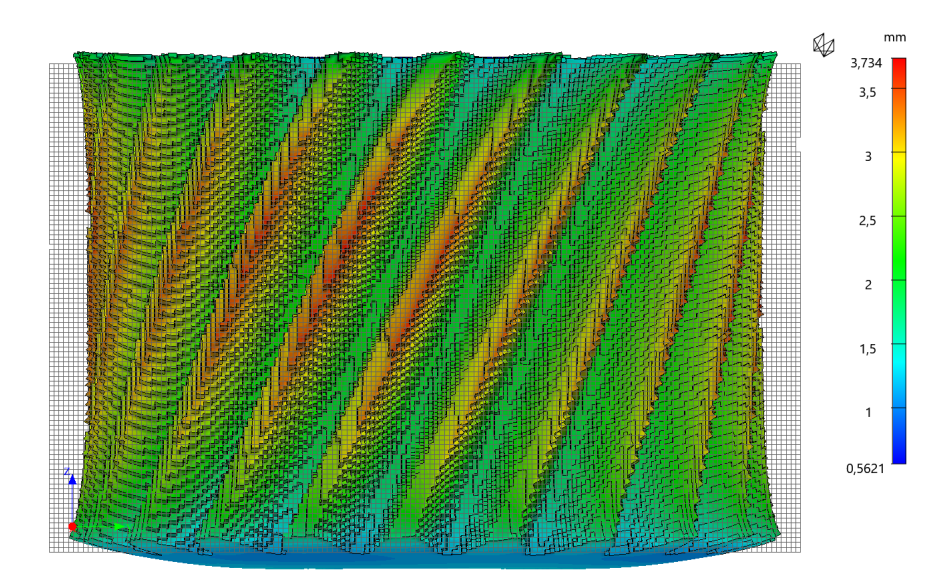


Figure 6.14: Exaggerated deformation visualisation on the FFF helical gear voxelized mesh

Figure 6.14 displays the deformation of the voxelized mesh of the helical gear realised by the FFF process. The deformation is exaggerated by a scale factor of 3 for clarity. The overall deformation trends are similar to those observed in the spur gear. As seen before, the lower face of the gear, placed on the printing bed, is curved upward with the edges lifted from the platform. In order to battle this, the compensated geometry will include a concave curvature on this face. This curvature is the root of the problem encountered in deformation minimisation for this part.

In contrast to the SLS process, the FFF process requires the generation of supports, usually when an overhang of about 45° is exceeded. According to the figure 6.15, realisation of the curvature on the bottom surface of the part requires a need for generation of support structures. While Digimat-AM has the ability to model the support structures implicitly or explicitly, changes in the supported area are needed after a new compensated geometry is generated. This acts as an external factor, altering the outcome of the simulations. In this study, the supports were modelled implicitly, based on a general overhang rule. An implicit model means the effect of the presence of a support structure is accounted for by the application of boundary conditions on the node face. After the support removal phase, placed before the annealing process, the boundary conditions are relaxed.

Ø

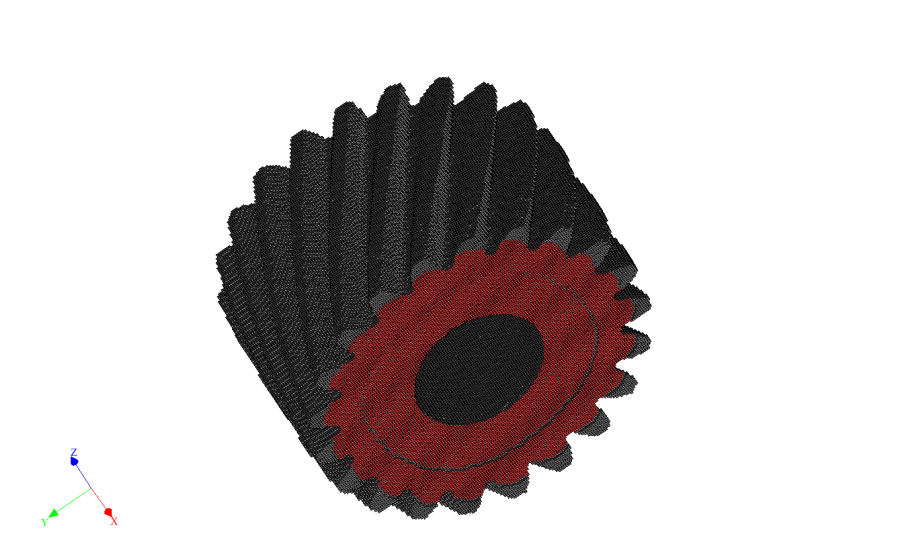


Figure 6.15: Visualisation of the voxelized mesh generated for the FFF helical gear. The red surface indicates a need for support structures.

Figure 6.16 shows the deformation observed on the bottom surface of the gear after manufacturing, when support structures are used.

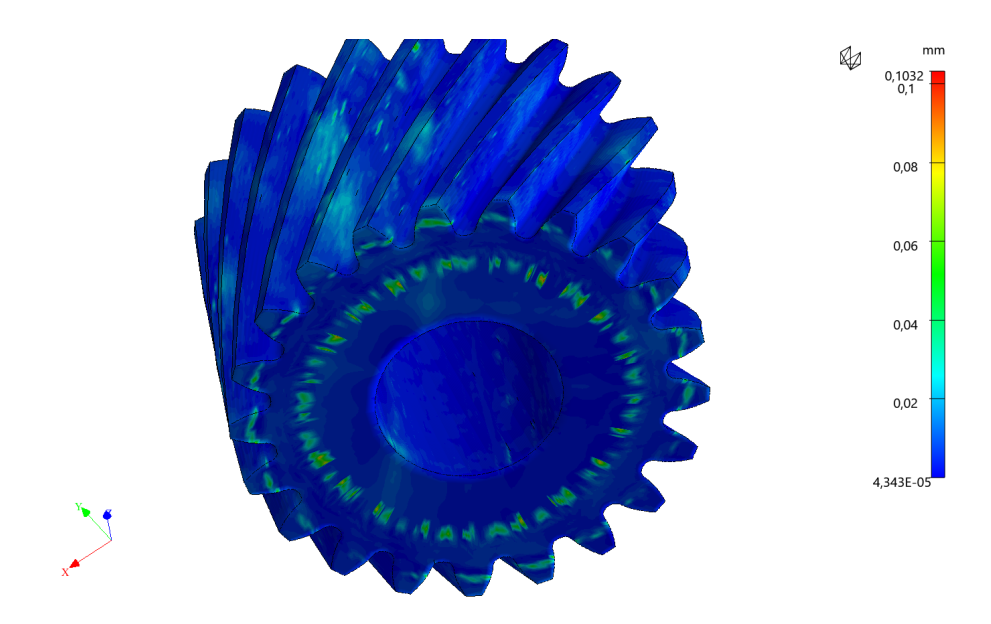


Figure 6.16: Deformation on the bottom face of the helical gear realised by FFF

Regarding the SLS process, the inclusion of annealing must be discussed first. In contrast to the spur gear, the helical gear produced using the SLS process contains high levels of residual stress, necessitating annealing. Annealing temperature and duration are kept the same as those used for the FFF Process. Figure 6.17 shows the effect of annealing on residual stress distribution. While the stress distribution remains remarkably similar to its pre-annealing state, the maximum value of residual stress is reduced by an order of magnitude.

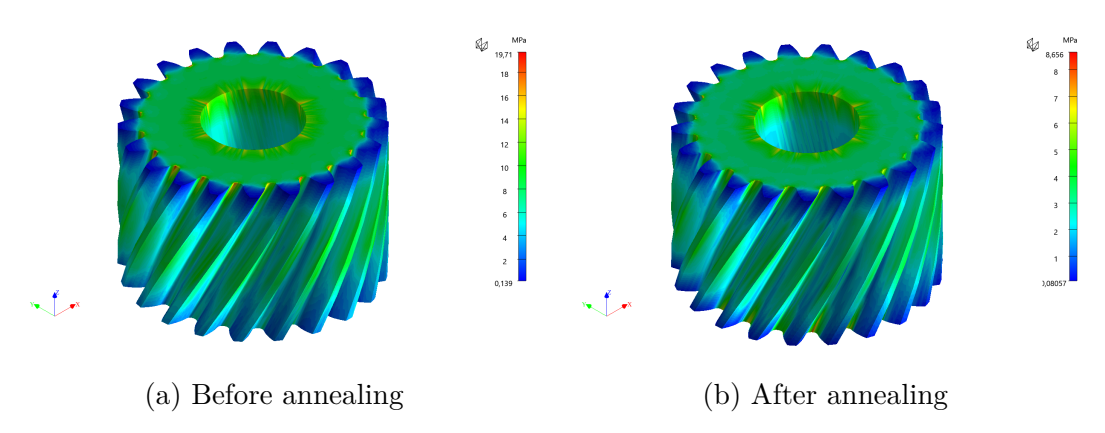


Figure 6.17: The effect of annealing on the residual stress in the helical gear manufactured by SLS

Figure 6.18 shows the comparison in the exaggerated deformation of the voxelized mesh before and after annealing. Before the annealing process, the helical gear realised using the SLS process shows the same deformation pattern seen in the spur gear. While the bottom face remains flat on the printing platform, the top face undergoes shrinkage. Interestingly, since the annealing process is performed after the removal of the part from the printing platform, it causes the bottom face to shrink equally. Overall, this results in the realisation of a part with almost uniform shrinkage. After annealing, the maximum warpage in the part remains at around

1 mm. That is the warpage, without considering the effects of uniform shrinkage.

Overall, since the annealed part, as seen in figure 6.18(b), shows an almost uniform shrinkage without any curvatures, the geometry compensation cycles perform remarkably well.

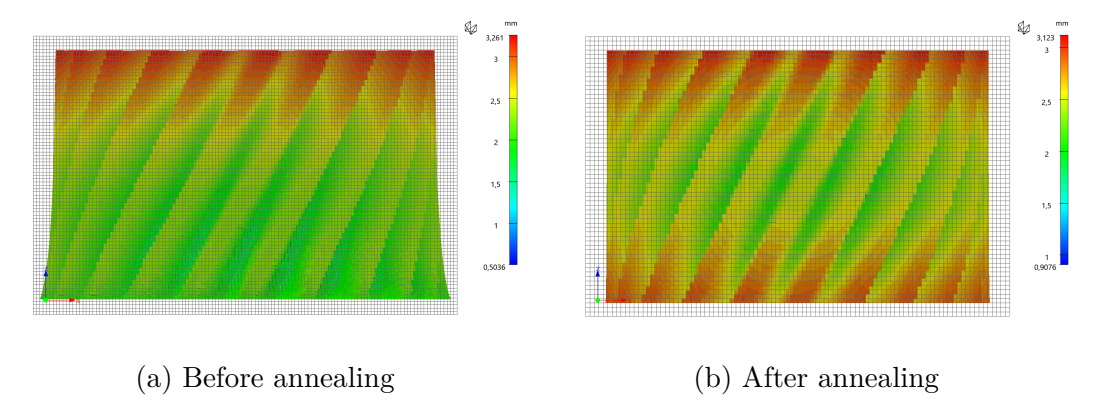


Figure 6.18: Exaggerated visualisation of the effect of annealing on the deformation of the helical gear manufactured by SLS

Figure 6.19 shows the final results obtained for the helical gear using the SLS process. As seen in the picture, the printed part is almost perfect.

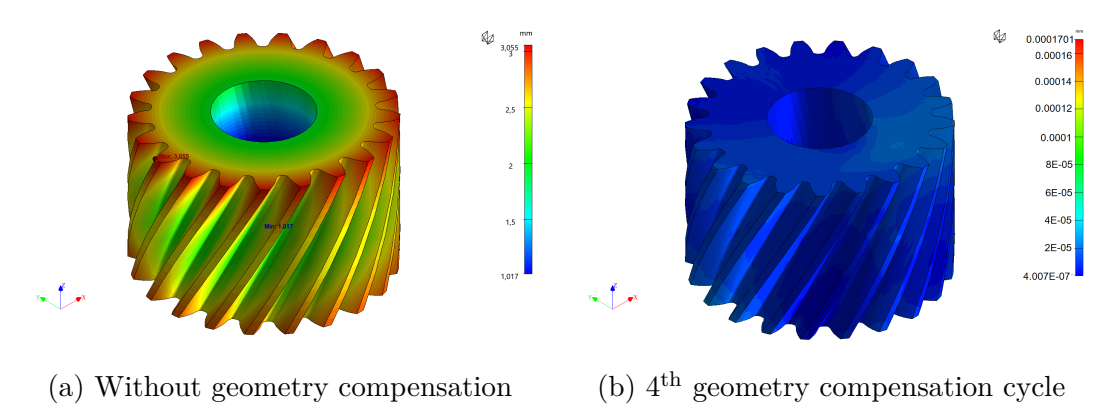


Figure 6.19: Total deviation from the as-designed geometry in SLS helical gear: before geometry compensation and after four cycles of geometry compensation.

Table 6.9 reports the maximum deformation with respect to the reference geometry, recorded after each geometry compensation cycle. The magnitude reduced consistently until the $4^{\rm th}$ geometry compensation cycle, and there was no need to keep going forward.

Table 6.9: Maximum deviation from the reference geometry in the annealed helical gear after successive compensation cycles in the SLS process

Run	Maximum Deviation
Base	$3.055\mathrm{mm}$
Cycle 1	$0.1230\mathrm{mm}$
Cycle 2	$0.006377\mathrm{mm}$
Cycle 3	$0.001093\mathrm{mm}$
Cycle 4	$0.0001701\mathrm{mm}$

6.8 Conclusion

To conclude, the geometrical accuracy was significantly improved for all parts. Although the tooth flank tolerance class will be formally evaluated in the next chapter, the present results already indicate that, except for the helical gear manufactured by the FFF process, the obtained geometries are expected to satisfy a defined tolerance class. In contrast, the deviations in the FFF helical gear are too large to justify such an evaluation.

For the SLS process, annealing proved to be highly beneficial for improving geometrical accuracy. It helped reduce shape deviations to very low levels; however, residual stresses were not fully eliminated, even after annealing. A higher annealing temperature or longer duration may be required to completely relieve the stresses.

For the spur gear realised with the SLS process, annealing was not applied due to the initially low levels of residual stress. At the time, it was not recognised that, even though annealing does not directly improve dimensional accuracy, it significantly improves the effectiveness of geometry compensation. This was realised only later; however, the previous simulations were not repeated. In this way, the study highlights the importance of annealing for compensation by contrasting cases where it was applied with those where it was not.

In the case of the FFF process, acceptable results were obtained for the spur gear. However, the results for the more complex and larger helical gear were not satisfactory. The issue arises from the changing support requirements for the bottom face of the print as the compensated geometry evolves. This external disturbance causes the residual deformation of the part to oscillate around $100\,\mu\text{m}$, rather than converging to a lower value. One possible solution to this issue would be to generate supports for the entire lower face of the gear, even on base geometry, and then keep the supports consistent across all subsequent compensation cycles, regardless of whether they are strictly required. Such consistency may help resolve the problem.

Chapter 7

ISO Tolerance Evaluation of Manufactured Gears

7.1 Introduction

To evaluate the achieved level of dimensional accuracy in manufactured gears, the ISO standards provide a reliable framework. In particular, the ISO system of flank tolerance classification defines the permissible deviations related to the flanks of gear teeth and establishes criteria for assessing manufacturing quality. While finite element method simulations directly yield results in terms of maximum deformations, these outcomes can be linked to dimensional accuracy requirements as specified in the relevant standards. Among them, ISO 1328-1:2013 serves as the definitive reference for flank tolerances. It presents a comprehensive system for defining, manufacturing, and assessing the conformity of tooth flanks in cylindrical involute gears.

This chapter outlines the methodology used for calculating tolerances, the requirements for gear measurement, and the criteria for verifying compliance with established tolerance classes.

7.2 Measurement Requirements

According to BS ISO 1328-1:2013, for gears within flank tolerance classes 7 to 11 and with a reference diameter (d) up to 4000 mm, a minimum set of five default parameters shall be measured and checked for compliance. These five parameters form the basis of conformity evaluation for the manufactured gears:

1. Single pitch deviation (f_p) : The single pitch deviation f_p is the maximum absolute value among all individual single pitch deviations f_{pi} . Each f_{pi} represents the difference between the actual and theoretical pitch of a tooth, measured at the pitch circle in the transverse plane. Its allowable tolerance, f_{pT} , depends on the reference diameter (d), the normal module (m_n) , and the flank tolerance class (A).

$$f_p = \max|f_{pi}| \tag{7.1}$$

2. Total cumulative pitch deviation (F_p) : The total cumulative pitch deviation F_p is defined as the largest algebraic difference between the individual cumulative pitch deviations F_{pi} for a specified flank, measured across all teeth of the gear. It represents the displacement of any tooth flank relative to a datum tooth flank. The allowable tolerance F_{pT} is calculated based on the reference diameter (d), the normal module (m_n) , and the flank tolerance class (A).

$$F_p = \max F_{pi} - \min F_{pi} \tag{7.2}$$

- 3. **Tooth thickness** (s): The parameter s represents the tooth thickness at the reference circle. A complete geometrical definition is provided in ISO 21771. The 1328-1 standard does not specify default tolerance limits for s, but it shall be verified when required by design drawings or purchase specifications.
- 4. Total profile deviation (F_{α}) : It is the distance between two parallel facsimiles of the design involute profile that fully enclose the measured profile over the evaluation range. Its tolerance $f_{\alpha T}$ is calculated by combining profile slope tolerance $(f_{H\alpha T})$ and profile form tolerance $(f_{f\alpha T})$, each depending on m_n , d, and class A.
- 5. Total helix deviation (F_{β}) : It is the distance between two parallel facsimiles of the design helix that fully enclose the measured helix across the facewidth. Its tolerance $F_{\beta T}$ is calculated from the helix slope deviation $(f_{H\beta})$ and helix form deviation $(f_{f\beta})$, depending on d, facewidth (b), and class A.

These five parameters form the *minimum required measurements* for conformity evaluation of gears in the relevant tolerance classes. The values obtained from gear inspection are compared against the calculated tolerances to determine the ISO accuracy class with which the gear complies.

Table 7.1: Summary of flank tolerances

Name	Symbol
Cumulative pitch tolerance, total	F_{PT}
Single pitch tolerance	f_{pT}
Profile slope tolerance	$f_{H lpha T}$
Profile form tolerance	$f_{f lpha T}$
Helix slope tolerance	$f_{Heta T}$
Helix form tolerance	$f_{feta T}$
Profile tolerance, total	$F_{lpha T}$
Helix tolerance, total	$F_{eta T}$

7.3 Class-Based Tolerance Calculation

For the spur gear, the class-based tolerances can be calculated based on the measurements reported in table 7.2.

Table 7.2: Geometrical characteristics of the spur gear

Parameter	Factor Levels
$\overline{\text{Module }(m)}$	3.0 mm
Normal Module (m_n)	$3.0\mathrm{mm}$
Face Width (b)	$10.0\mathrm{mm}$
Reference Diameter (d)	$33.0\mathrm{mm}$
Tip Diameter (d_a)	$40.8\mathrm{mm}$
Measurement Diameter (d_M)	$34.8\mathrm{mm}$
Theoretical Pitch $(P_t m)$	$9.935\mathrm{mm}$
Number of Teeth (z)	11
Profile Shift (x)	0.3
Considered Flank Tolerance Classes (A)	7 to 11

Table 7.3 reports the allowable tolerances calculated for the spur gear by applying the formulae from the BS ISO 1328-1:2013 standard, based on gear dimensions. The values are rounded, according to the specific directions given by the same document.

Table 7.3: Calculated tolerance values for tooth flank tolerance classes 7–11

Class A	f_{pT}	F_{pT}	$F_{lpha T}$	$F_{eta T}$
	$(\mu \mathrm{m})$	$(\mu \mathrm{m})$	$(\mu \mathrm{m})$	$(\mu \mathrm{m})$
7	12	35	17	10
8	18	49	24	15
9	25	69	34	21
10	35	98	48	30
11	50	139	68	42

7.4 Shape deviation measurements

7.4.1 Single and Cumulative Pitch Deviation

Based on the guidelines of ISO 1328-1:2013, the theoretical pitch of the gear is calculated as 9.935 mm. The actual pitch must be measured on the midplane of the gear. To perform this measurement, the warped geometry is exported as an STL file and analysed in Autodesk Inventor. The mesh representing the flank surface of each tooth can be converted into a surface, and the intersection of this surface with the midplane provides the warped tooth flank profiles. The pitch is measured on the measurement diameter, and the values of f_p are simply calculated based on the difference between the theoretical and measured pitch value and rounded according to ISO instructions.

Table 7.4: Measured pitch and single pitch deviation (f_{pi}) for each tooth of the spur gear produced by FFF

Tooth i	Right Flank		Left Fla	ank
	Measured Pitch (mm)	f_{pi} (μ m)	Measured Pitch (mm)	f_{pi} (μ m)
1	9.9450	2	9.9385	4
2	9.9397	-4	9.9376	3
3	9.9471	1	9.9363	2
4	9.9461	1	9.9337	-1
5	9.9486	8	9.9379	3
6	9.9368	0	9.9383	4
7	9.9303	10	9.9398	5
8	9.9351	5	9.9432	9
9	9.9355	13	9.9353	1
10	9.9421	12	9.9485	14
11	9.9345	14	9.9320	-3

Table 7.5: Measured pitch and single pitch deviation (f_{pi}) for each tooth of the spur gear produced by SLS

Tooth i	Right Flank		Left Fla	ınk
	Measured Pitch (mm)	f_{pi} (μ m)	Measured Pitch (mm)	f_{pi} (μ m)
1	9.9384	-1	9.9362	2
2	9.9329	-3	9.9353	1
3	9.9379	-1	9.9343	0
4	9.9344	3	9.9317	-3
5	9.9317	1	9.9325	-2
6	9.9337	-2	9.9343	0
7	9.9313	4	9.9341	0
8	9.9340	-2	9.9370	2
9	9.9378	3	9.9342	0
10	9.9360	0	9.9378	3
11	9.9323	-3	9.9330	-2

According to formula 7.1 and tables 7.4 and 7.5, f_p can be readily calculated for samples printed by different processes. For the FFF process, f_p is equal to 14 µm, while it's equal to 4 µm for the SLS process.

According to the standard, F_{pi} is, in theory, equal to the algebraic sum of the individual single pitch deviations f_{pi} over the same n pitches. Hence, F_{pi} over

n=1,2,...,11 is calculate based on the data from tables 7.4 and 7.5. After application of equation 7.2, it is equal to 69 µm for the FFF, and 16 µm for the SLS part. Table 7.6 summarises the findings of pitch measurements.

Table 7.6: Summary of pitch deviations in the spur gear

Technology	$f_p \; (\mu \mathrm{m})$	$F_p \; (\mu \mathrm{m})$
SLS	4	16
FFF	14	69

7.4.2 Profile Deviation, Total

The facsimiles of the design profile are obtained from the initial part and compared to the design profile of the warped geometry. Total profile deviation is the distance between two facsimiles of the design profile, which can contain the tooth profile. Table 7.7 reports the individual deviations measured on each flank of the gear geometries obtained by reach technology.

Table 7.7: Measured profile deviation F_{α} for SLS and FFF parts

Tooth i	SLS $F_{\alpha}i$ (µm)		FFF F_{α}	<i>i</i> (μm)
-	Left Flank	Right Flank	Left Flank	Right Flank
1	13	13	13	21
2	2	2	8	26
3	13	11	13	21
4	2	4	17	34
5	19	21	30	21
6	2	0	30	13
7	13	15	21	34
8	6	11	26	30
9	4	2	26	26
10	11	13	26	17
11	0	2	13	8

Table 7.8 reports the maximum deviation observed for each geometry, which must be compared to table 7.3 for determination of the tolerance class.

Table 7.8: Summary of profile deviations in the spur gear

Technology	$m{f}_{lpha}~(m{\mu}{ m m})$
SLS	21
FFF	34

7.4.3 Helix Deviation, Total

The helix deviation is measured similarly to the profile deviation. The helix design facsimiles are obtained based on the designed geometry's flank surface. The warped flank surface is contained between two facsimiles of the designed helix, and the distances are measured. The measurements are reported in table 7.9 for both technologies.

Table 7.9: Measured profile deviation F_{β} for SLS and FFF parts

Tooth i	SLS $F_{\beta}i$ (μm)		FFF F_{β}	<i>i</i> (μm)
	Left Flank	Right Flank	Left Flank	Right Flank
1	17	12	29	27
2	18	14	36	31
3	18	20	35	35
4	15	15	36	16
5	19	18	18	27
6	15	14	29	36
7	15	18	30	32
8	14	17	36	33
9	14	17	21	34
10	25	18	23	32
11	13	16	23	27

For each technology, the maximum measured helix deviation is reported in table 7.9, giving the tolerance class when compared to table 7.3.

Table 7.10: Summary of helix deviations in the spur gear

Technology	$oldsymbol{f}_eta \; (oldsymbol{\mu} \mathrm{m})$
SLS	25
FFF	36

7.4.4 Achieved Tolerance Classes

Tables 7.11 and 7.12 report the tolerance classes achieved based on each individual measurement made on geometries obtained from either technology. The tooth flank tolerance of a gear is equal to the highest tolerance class achieved. Therefore, it is equal to class 10 for the SLS and class 11 for the FFF part.

Table 7.11: Tolerance classes for SLS

Table 7.12: Tolerance classes for FFF

Parameter	Tolerance	parameter	Tolerance
	Class		Class
$\overline{f_p}$	7	$\overline{f_p}$	8
F_p	7	F_p	9
F_{lpha}	8	F_{lpha}	9
F_{eta}	10	F_eta	11

7.5 Extension to the Helical Gears

A full ISO tolerance evaluation was carried out for the spur gear, as presented in the previous sections. For the helical gear, the same methodology would in principle be applied. However, two considerations justify not performing the detailed analysis here.

First, for the FFF helical gear, the dimensional deviations are so large that the part would not fall into any defined ISO tolerance class. Therefore, a full evaluation would not provide meaningful results.

Second, for the SLS helical gear, the dimensional deviations are minimal. The part demonstrates very high geometrical fidelity and would readily satisfy the requirements for the highest ISO accuracy classes across all evaluated parameters. A detailed parameter-by-parameter analysis is therefore unnecessary, since its conformity is already evident. However, it must be emphasised that geometrical accuracy alone does not fully define gear quality. Other aspects, such as surface roughness, the integrity of the load-bearing flanks, and the distribution of residual stresses, play equally important roles in determining performance. These factors, while crucial in practical applications, are outside the scope of this thesis, which focuses primarily on dimensional accuracy and flank tolerance classification.

7.6 Conclusion

This chapter applied the ISO 1328-1:2013 system to assess the dimensional accuracy of additively manufactured gears. For the spur gear, detailed tolerance calculations were performed, showing that both technologies achieved comparable results, with the SLS part reaching class 10 accuracy and the FFF part reaching class 11.

For the helical gear, the full ISO analysis was not repeated, since the outcome is already clear: the deviations in the FFF gear are too large for it to fall into any tolerance class, while the SLS gear achieves values consistent with the lower ISO classes. The contrast between the two processes becomes much more pronounced in the helical gear case, and the underlying causes of these deviations were analysed in detail in Chapter 6. Moreover, according to the standard, the measurements must be carried out on a physical part, and for the helical gear, which may fall into a tolerance class lower than 7, it is uncertain whether digital tools such as CAD software and

STL-based analysis provide sufficient accuracy to yield a reliable assessment.

Overall, the ISO evaluation highlights that both technologies can deliver similar accuracy for smaller, simpler gears, but their performance diverges significantly for more complex geometries. This underscores the importance of considering part complexity when evaluating the suitability of different additive manufacturing processes for gear production.

Chapter 8

Conclusions and Future Work

8.1 Summary of Findings

This thesis set out to develop a workflow for improving the dimensional accuracy of polymer parts manufactured by selective laser sintering and fused filament fabrication. Gears were chosen as representative case studies. The work first focused on improving accuracy through the optimisation of process parameters and finding the relative importance of different factors. The application of annealing was considered when applicable. Subsequently, the geometry compensation capabilities of Digimat were evaluated and implemented to bring the manufactured shape closer to the original design. Finally, the dimensional accuracy of the parts was assessed in practical terms using ISO standards for tooth flank tolerances.

Optimised Process Parameters

The following process parameter levels were found to decrease deformations for a small spur gear manufactured using PA12 material.

Fused Filament Fabrication

• Layer thickness: 0.2 mm

• Extrusion temperature: 240 °C

• Deposition speed: $100 \,\mathrm{mm}\,\mathrm{s}^{-1}$

• Infill density: $20\,\%$

• Bed temperature: 90 °C

Selective Laser Sintering

• Chamber temperature: 180 °C

• Volumetric energy density: 0.16 J mm⁻²

Annealing

• Temperature: 150 °C

• Time: 12 h

Key Insights

- In FFF, the infill density is the most significant contributor to the part deformation, followed by extrusion temperature and layer thickness, which also have a major influence on the residual stress levels.
- In SLS, chamber temperature has the most influence on deformation and residual stresses.
- For the annealing process, the influence of temperature is much more pronounced with respect to the duration.
- Annealing enhances the effectiveness of geometry compensation, especially for SLS.

For the spur gear, both manufacturing processes achieved comparable results. After optimisation and compensation, the FFF part reached an ISO tolerance class of 11 with a maximum deviation of $0.04265\,\mathrm{mm}$, while the SLS part achieved class 10 with a maximum deviation of $0.007317\,\mathrm{mm}$.

For the helical gear, the performance of different technologies diverged significantly. When annealing was used, the geometry compensation was able to reduce the maximum deformation in the SLS gear to extremely low values. In the case of the FFF process, on the other hand, it was not possible to decrease the deformations below 0.09737 mm. This is likely due to the requirement of support structures in the FFF process, which disturbed the geometry compensation workflow.

8.2 Contributions of the Thesis

While the literature review shows that simulation is often applied to study the influence of process parameters on part accuracy, this thesis extended the methodology to a complex and functionally relevant part rather than simple benchmark geometries. By considering gear samples, a practical workflow was developed and tested on a real application. The choice of gears also made it possible to assess dimensional accuracy in reference to standardised ISO tolerance classes, providing a more meaningful evaluation. In addition, the study included annealing as a factor alongside process parameters, highlighting its role in reducing residual stresses and improving the effectiveness of geometry compensation.

The thesis contributes a workflow that integrates finite element simulations, geometry compensation, and post-processing strategies to systematically improve dimensional accuracy. Using Taguchi and full factorial design of experiments, the

influence of key parameters was quantified for both FFF and SLS. The results showed that different mechanisms govern deformation in the two processes, with infill density and extrusion temperature dominating in FFF, while chamber temperature and volumetric energy density are critical in SLS. Geometry compensation was shown to progressively reduce deviations, though challenges such as oscillatory behaviour in FFF helical gears remain.

Finally, the work introduced a digital methodology for assessing ISO tooth flank tolerances directly from STL files. This allowed prediction of tolerance classes prior to manufacturing, although the method proved more reliable for spur gears than for complex geometries such as FFF helicals. Together, these contributions provide practical guidance for selecting process parameters, applying post-processing, and interpreting digital evaluations, offering a step toward more predictable and accurate gear production with additive manufacturing.

8.3 Suggestions for Future Research

Future work could address several limitations and extend the methodology:

- Experimental Validation: While this thesis relied on simulations, physically printing and measuring the gears would confirm the predicted deformations and validate the digital ISO evaluation approach. This step is particularly important for complex geometries, where STL-based assessment may be less reliable.
- Support Structure Strategies for FFF: The oscillatory deformation observed in FFF helical gears' geometry compensation cycles highlights the need for more robust support design. Future work could explore consistent support strategies across all compensation cycles or the use of more advanced compensation algorithms that account for evolving support requirements. Including supports from the beginning, even if they are not strictly needed, may also help improve convergence and reduce residual deformation.
- Annealing Optimisation: For larger SLS gears, investigating higher temperatures or longer annealing durations could further reduce residual stresses while maintaining dimensional stability.
- Mechanical Performance Assessment: While a low infill density (20%) was found to improve dimensional accuracy in FFF parts, its impact on mechanical strength and functional performance remains unclear. Future work should experimentally evaluate these aspects to ensure that geometry optimisation does not compromise part functionality.
- Secondary Effects: While this study focused on shrinkage, warpage, and residual stress, Digimat allows for the evaluation of secondary effects, too. In particular, for the SLS process, it is also possible to measure the degree of

sintering and the degree of crystallinity. For the FFF process, on the other hand, porosity can be studied. For example, Figure 8.1 shows the degree of sintering in the SLS process, before and after geometry compensation is used. In this case, the sharper edges and curvatures obtained by the geometry compensation might compromise sintering. In the future, the effects of process parameters, as well as the simulation set-up, the mesh size, for instance, on these phenomena might be studied.

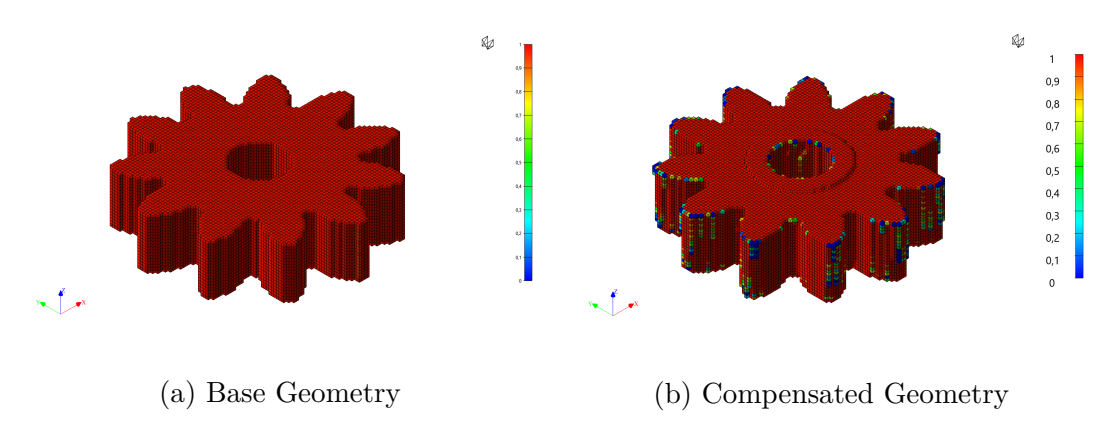


Figure 8.1: The effect of the degree of sintering on geometry compensation

8.4 Closing Remarks

The developed methodologies, combining high-fidelity simulations, digital ISO tolerance evaluation, and compensation cycles, provide a predictive framework that reduces trial-and-error experimentation. They improve understanding of process and geometry interactions and support future work on complex parts, adaptive compensation strategies, and experimental validation to ensure dimensional accuracy without compromising mechanical performance.

Bibliography

- [1] Ngo T.D., Kashani A., Imbalzano G., Nguyen K.T.Q., and Hui D. "Additive manufacturing (3D printing): A review of materials, methods, applications and challenges". In: *Composites Part B: Engineering* 143 (Nov. 2018), pp. 172–196 (cit. on pp. 1, 4).
- [2] Vasco J.C. *Handbooks in Advanced Manufacturing*. Ed. by Pou J., Riveiro A., and Davim J.P. Amsterdam, Netherlands: Elsevier, 2021 (cit. on p. 1).
- [3] Zanini A., Marconi M., and Rubino G. "Analysing shrinkage compensation in additive manufacturing: a comparative study of reverse engineering and gauge-based methods". In: *Proceedings of the Design Society.* 2024 (cit. on p. 2).
- [4] Scott A. "A review of melt extrusion additive manufacturing processes: II. Materials, dimensional accuracy, and surface roughness". In: *Rapid Prototyping Journal* 21 (Nov. 2015), pp. 250–261 (cit. on p. 2).
- [5] Zhang F., Zhu L., Li Z., Wang S., Shi J., Tang W., Li N., and Yang J. "The Recent Development of Vat Photopolymerization: A Review". In: Additive Manufacturing 48 (2021), p. 102423. ISSN: 2214-8604. DOI: 10.1016/j.addma. 2021.102423 (cit. on p. 4).
- [6] Islam M.A., Mobarak M.H., Rimon M.I.H., Al Mahmud M.Z., Ghosh J., Ahmed M.M.S., and Hossain N. "Additive Manufacturing in Polymer Research: Advances, Synthesis, and Applications". In: *Polymer Testing* 132 (2024), p. 108364. DOI: 10.1016/j.polymertesting.2024.108364 (cit. on p. 4).
- [7] Elkaseer A., Chen K.J., Janhsen J.C., Refle O., Hagenmeyer V., and Scholz S.G. "Material Jetting for Advanced Applications: A State-of-the-Art Review, Gaps and Future Directions". In: *Additive Manufacturing* 60 (2022), p. 103270. ISSN: 2214-8604. DOI: 10.1016/j.addma.2022.103270 (cit. on p. 4).
- [8] Li M., Du W., Elwany A., Pei Z., and Ma C. "Metal Binder Jetting Additive Manufacturing: A Literature Review". In: *Journal of Manufacturing Science and Engineering* 1 (2020) (cit. on p. 5).
- [9] Mwania F.M., Maringa M., and van der Walt J.G. "A review of the techniques used to characterize laser sintering of polymeric powders for use and re-use in additive manufacturing". In: *Additive Manufacturing* (2021) (cit. on p. 5).

- [10] Fico D., Rizzo D., Casciaro R., and Corcione C.E. "A Review of Polymer-Based Materials for Fused Filament Fabrication (FFF): Focus on Sustainability and Recycled Materials". In: *Materials* (2022) (cit. on p. 5).
- [11] Alzyod H. and Ficzere P. "Material-Dependent Effect of Common Printing Parameters on Residual Stress and Warpage Deformation in 3D Printing: A Comprehensive Finite Element Analysis Study". In: *Polymers* 15.13 (2023), p. 2893. DOI: 10.3390/polym15132893 (cit. on pp. 5–7, 20).
- [12] Porcaro R., Fontana F., Ciotti M., et al. "Warpage evaluation and mechanical characterisation of modified polyamide-6 specimens produced by Arburg plastic freeformer". In: *Progress in Additive Manufacturing* 10 (2025), pp. 2383–2395. DOI: 10.1007/s40964-024-00756-0 (cit. on pp. 5, 6).
- [13] Alzyod H. and Ficzere P. "Optimizing fused filament fabrication process parameters for quality enhancement of PA12 parts using numerical modeling and Taguchi method". In: *Heliyon* 9.3 (2023), e14445. DOI: 10.1016/j.heliyon. 2023.e14445 (cit. on pp. 5–7, 10, 20, 21).
- [14] Sreejith P., Patterson A.E., Rajagopal K.R., and Vajipeyajula B. "Process-induced shrinking and warping in additively manufactured polycarbonate plates". In: *Applications in Engineering Science* 22 (2025), p. 100220. ISSN: 2666-4968. DOI: 10.1016/j.apples.2025.100220 (cit. on pp. 5–7).
- [15] Nyiranzeyimana G., Mutua J.M., Mbuya T.O., and Mose B.R. "Optimization of fused deposition modelling process parameters and the effect on residual stresses of built parts". In: *Materials Today: Proceedings* 66.5 (2022), pp. 2914–2918. DOI: 10.1016/j.matpr.2022.06.557 (cit. on pp. 6, 7).
- [16] Ahmadi Dastjerdi A., Movahhedy M.R., and Akbari J. "Optimization of process parameters for reducing warpage in selective laser sintering of polymer parts". In: *Additive Manufacturing* 18 (2017), pp. 285–294. DOI: 10.1016/j.addma. 2017.10.018 (cit. on pp. 6–8).
- [17] Ren N.F., Wang P., Luo Y., and Wu H.J. "Experimental Study on Warping Height of PA12/HDPE Specimen by Selective Laser Sintering". In: *Applied Mechanics and Materials* 43 (2011), pp. 430–433. DOI: 10.4028/www.scientific.net/AMM.43.430 (cit. on pp. 6–8).
- [18] Yan R., Xie C., Zhao Z., and Li J. "Optimization of Selective Laser Sintering Process Parameters Based on PA12 Powders for Bone Tissue Scaffolds". In: 3D Printing and Additive Manufacturing 10.5 (2023), pp. 1064–1071. DOI: 10.1089/3dp.2021.0111 (cit. on pp. 6, 8).
- [19] Jabri F.E., Ouballouch A., Lasri L., and El Alaiji R. "A comprehensive review of polymer materials and selective laser sintering technology for 3D printing". In: Journal of Achievements in Materials and Manufacturing Engineering 118.1 (2023), pp. 5–17. DOI: 10.5604/01.3001.0053.7286 (cit. on p. 8).

- [20] Ruggi D., Lupo M., Sofia D., Barrès C., Barletta D., and Poletto M. "Flow properties of polymeric powders for selective laser sintering". In: *Powder Technology* 370 (2020), pp. 288–297. DOI: 10.1016/j.powtec.2020.05.069 (cit. on p. 8).
- [21] Zhao Y., Li M., Chen J., and Zeng Y. "Performance Improvement of Additively Manufactured Complex Configuration of Polyamide 12". In: *Additive Manufacturing Frontiers* 3.4 (2024), p. 200165. DOI: 10.1016/j.amf.2024.200165 (cit. on p. 10).
- [22] Ferreira I., Melo C., Neto R., Machado M., Alves J.L., and Mould S. "Study of the annealing influence on the mechanical performance of PA12 and PA12 fibre reinforced FFF printed specimens". In: *Rapid Prototyping Journal* 26.10 (2020), pp. 1761–1770. DOI: 10.1108/RPJ-10-2019-0278 (cit. on pp. 10, 20, 22).
- [23] Liu X., Tey W.S., Choo J.Y.C., Chen J., Tan P., Cai C., Ong A., Zhao L., and Zhou K. "Enhancing the mechanical strength of Multi Jet Fusion-printed polyamide 12 and its glass fiber-reinforced composite via high-temperature annealing". In: *Additive Manufacturing* 46 (2021), p. 102205. DOI: 10.1016/j.addma.2021.102205 (cit. on p. 10).
- [24] Zhang H., Liang M., Yao J., Cao Y., Wang Y., Wu D., Liu X., Fu Q., and Sun Y. "Effect of Annealing on Structure and Mechanical Properties of 3D-Printed Polymer Composites". In: *Polymer Composites* (2025). DOI: 10.1002/pc.70286 (cit. on p. 10).
- [25] Papazoglou E.L., Karkalos N.E., Karmiris-Obratański P., Manolakos D.E., and Salonitis K. "On the Modeling and Simulation of SLM and SLS for Metal and Polymer Powders: A Review". In: *Archives of Computational Methods in Engineering* 29 (2022), pp. 941–973. DOI: 10.1007/s11831-021-09601-x (cit. on p. 10).
- [26] Behseresht S., Park Y.H., Love A., and Valdez Pastrana O.A. "Application of Numerical Modeling and Finite Element Analysis in Fused Filament Fabrication: A Review". In: *Materials* 17.17 (2024), p. 4185. DOI: 10.3390/ma17174185 (cit. on p. 10).
- [27] Sharafi S., Santare M.H., Gerdes J., and Advani S.G. "A multiscale modeling approach of the Fused Filament Fabrication process to predict the mechanical response of 3D printed parts". In: *Additive Manufacturing* 51 (2022), p. 102597. DOI: 10.1016/j.addma.2022.102597 (cit. on p. 10).
- [28] Alzyod H. and Ficzere P. "Using Numerical Simulation to Investigate the Effect of Layer Thickness on Residual Stress and Warping of Specimens Made of ABS". In: *Design of Machines and Structures* 12.1 (2022), pp. 5–11. DOI: 10.32972/dms.2022.001 (cit. on pp. 10, 20).

- [29] Khanjar S. "Digital Design and Thermomechanical Process Simulation for 3D Printing with ABS and Soyhull Fibers Reinforced ABS Composites". Master's Thesis. University of Louisville, Dec. 2021. DOI: 10.18297/etd/3786 (cit. on p. 10).
- [30] Al Rashid A. and Koç M. "Numerical simulations on thermomechanical performance of 3D printed chopped carbon fiber-reinforced polyamide-6 composites: Effect of infill design". In: *Journal of Applied Polymer Science* 139.44 (2022), e53081. DOI: 10.1002/app.53081 (cit. on p. 11).
- [31] Castelló-Pedrero P., García-Gascón C., and García-Manrique J.A. "Multiscale numerical modeling of large-format additive manufacturing processes using carbon fiber reinforced polymer for digital twin applications". In: *International Journal of Materials Forming* 17 (2024), p. 15. DOI: 10.1007/s12289-024-01811-5 (cit. on p. 11).
- [32] Calignano F., Bove A., Mercurio V., and Marchiandi G. "Effect of Recycled Powder and Gear Profile on the Functionality of Additive Manufacturing Polymer Gears". In: *Rapid Prototyping Journal* 30.11 (2024), pp. 16–31. DOI: 10.1108/RPJ-06-2023-0199 (cit. on p. 11).
- [33] Zhang Y., Mao K., Leigh S., Shah A., Chao Z., and Ma G. "A Parametric Study of 3D Printed Polymer Gears". In: *The International Journal of Advanced Manufacturing Technology* 107.11–12 (2020), pp. 4481–4492. DOI: 10.1007/s00170-020-05270-5 (cit. on p. 11).
- [34] Hriberšek M., Kulovec S., Ikram A., Kern M., Kastelic L., and Pušavec F. "Technological optimization and fatigue evaluation of carbon reinforced polyamide 3D printed gears". In: *Heliyon* 10.13 (2024), e34037. DOI: 10.1016/j.heliyon. 2024.e34037 (cit. on p. 11).
- [35] Gupta K. "Recent Developments in Additive Manufacturing of Gears: A Review". In: Advances in Transdisciplinary Engineering, Volume 8: Advances in Manufacturing Technology XXXII (Proceedings of the 16th International Conference on Manufacturing Research, ICMR 2018). Ed. by Thorvald P. and Case K. IOS Press, 2018, pp. 131–136. DOI: 10.3233/978-1-61499-902-7-131 (cit. on p. 11).
- [36] Hexagon Manufacturing Intelligence. Digimat 2024.2 AM User's Guide. Hexagon MI. 2024. URL: https://nexus.hexagon.com/documentationcenter/en-US/bundle/Digimat_2024.2_AM_User_Guide/resource/Digimat_2024.2_AM_User_Guide.pdf (cit. on pp. 12, 13).
- [37] LLC Minitab. Getting Started with Minitab Statistical Software. Version 24.0 (obtained via Minitab documentation portal). Minitab, LLC. 2024. URL: https://www.minitab.com/content/dam/www/en/uploadedfiles/documents/getting-started/MinitabGettingStarted-v032024_EN.pdf (cit. on p. 14).
- [38] Roy R.K. A Primer on the Taguchi Method. 2nd. Society of Manufacturing Engineers, 2010 (cit. on p. 20).

- [39] Espino M.T., Tuazon B.J., Espera A.H. Jr., Nocheseda C.J.C., Manalang R.S., Dizon J.R.C., and Advincula R.C. "Statistical methods for design and testing of 3D-printed polymers". In: *MRS Communications* 13.2 (2023), pp. 193–211. DOI: 10.1557/s43579-023-00332-7 (cit. on pp. 20, 21).
- [40] Verim Ö., Saeed O., Eid M.H., et al. "Investigation of the effects of 3D printing parameters on mechanical tests of PLA parts produced by MEX 3D printing using Taguchi method". In: *Scientific Reports* 15 (2025), p. 15008. DOI: 10.1038/s41598-025-98832-0 (cit. on p. 21).

Dedications

To my family, whose sacrifices and support made it possible for me to grow and follow my dreams.

To all the friends I have met along this journey and with whom I have shared lasting memories, whose presence, encouragement, and companionship helped me reach this milestone.

And to all the kind and talented students of Politecnico di Torino, who inspired me every day with their dedication and drive.